Quantum Algorithms for the Study of Electronic Structure and Molecular Dynamics: Novel Computational Protocols

Srinivasan S Iyengar, Debadrita Saha, Anurag Dwivedi, Miguel A Lopez-Ruiz, Anup Kumar, Juncheng (Harry) Zhang, and Timothy C Ricard, Department of Chemistry, Department of Physics, and the Indiana University Quantum Science and Engineering Center (IU-QSEC), Indiana University, Bloomington, IN, United States

Philip Richerme, Department of Physics, and the Indiana University Quantum Science and Engineering Center (IU-QSEC), Indiana University, Bloomington, IN, United States

Amr Sabry, Department of Computer Science, School of Informatics, Computing, and Engineering, and the Indiana University Quantum Science and Engineering Center (IU-QSEC), Indiana University, Bloomington, IN, United States

Abstract

The accurate computational determination of chemical, materials, biological, and atmospheric properties has critical impact on a wide range of health and environmental problems, but is deeply limited by the computational scaling of quantum-mechanical methods. The complexity of quantum-chemical studies arises from the steep algebraic scaling of electron correlation methods, and the exponential scaling in studying nuclear dynamics and molecular flexibility. In this article we provide an overview of the challenges involved in performing accurate post-Hartree-Fock electronic structure and quantum nuclear dynamics calculations on quantum hardware. For electronic structure, we present a procedure to drastically reduce the depth of quantum circuits and improve the accuracy of results in computing post-Hartree-Fock electronic structure energies for large molecular systems. The method is based on molecular fragmentation where a molecular system is divided into overlapping fragments through a graph theoretic procedure. This allows us to create a set of projection operators that decompose the unitary evolution of the full system into separate sets of unitary processes, some of which can be treated on quantum hardware and others on classical hardware. Thus, we develop a procedure for electronic structure that can be asynchronously spawned on to a potentially large ensemble of classical and quantum hardware systems. We also discuss a framework which allows for the solution of quantum chemical nuclear dynamics by mapping these to quantum spin-lattice simulators. This mapping procedure allows us to determine the local fields and spin-spin couplings needed to identically match the molecular and spin-lattice Hamiltonians and hence the resultant dynamics.

doi:10.1016/B978-0-12-821978-2.00139-2

Key Points

- Quantum chemical dynamics simulations are severely hindered by the computational complexities of obtaining accurate potential energy surfaces and of performing quantum nuclear propagation.
- Electronic structure simulations are held back by the need for exponential increase in circuit depth in current quantum algorithms, causing significant propagation of errors.
- Graph theory based projection of quantum circuits, or quantum circuit fragmentation, can provide an approach to curtail circuit depth, provide quantum circuit based many-body approximations and control accuracy.
- The complexity in performing quantum chemical dynamics increases exponentially with the number of quantum nuclear dimensions.
- Control maps between quantum chemical dynamics Hamiltonians and spin-lattice Hamiltonians can be used for simulation of nuclear dynamics.
- Asynchronous and parallel quantum algorithms that seamlessly integrate classical and quantum architectures, such as those discussed here, may yield improved simulation of dynamics and structure.

1 Introduction

Computing accurate molecular properties, including the effect of electron correlation and nuclear dynamics, is at the heart of modern computational quantum chemistry, with potential impact on materials discovery,[1–3] and the accurate study of biological[4–10] and atmospheric[11–13] processes. However, such studies are deeply confounded by (a) the steep algebraic computational scaling of accurate electron correlation methods,[14–17] where, for example the gold standard of electronic structure theory, namely CCSD(T)[15,18] scales as $\mathcal{O}(N^{6-7})$, and (b) the exponential scaling of quantum nuclear dynamics with its degrees of freedom.[19] Over the years several classical algorithms have been developed to improve the computational scaling of both problems.[20–24] Orthogonally, the promise of solving exponentially complex problems efficiently using novel quantum computing hardware and associated software is a rapidly evolving research frontier,[25,26] and there are already diverse set of important scientific and technological challenges in artificial photosynthesis, computational catalysis, and structure-based drug design or vaccine development for human health that can benefit from such developments.

In this article, we discuss critical challenges for developing quantum algorithms for modeling complex chemical processes. This article is organized as follows: In Section 2 we discuss quantum computing for electronic structure methods, whereas in Section 3 we discuss mapping protocols for quantum nuclear dynamics and spectroscopy. Chemical problems studied using these approaches are summarized in Sections 4 and 5, and conclusions and future directions are given in Section 6.

2 Quantum Computing Methods for Electronic Structure

Recently, multiple quantum computing technologies, such as ion-traps,[27–30] superconducting coils,[31,32] Bosonic processors with photons,[36,39] solid-state devices and quantum dots inside cavities,[36,39] and Rydberg atoms[40–42] have emerged as potential alternative computational platforms to address complex computational challenges. Additionally, algorithms to approximate electron correlation problems,[43–64] for small molecular systems, and quantum nuclear dynamics problems[65–72] have been implemented on quantum hardware devices. The mapping of most electron correlation problems to quantum hardware is facilitated by the Jordan-Wigner, parity, or Bravyi-Kitaev transformations,[73–75] where a product of Fermionic creation and annihilation operators, as these arise within a second quantized version of the electronic Hamiltonian, are transformed to a chain of Pauli spin operators. Many groups[43,44,51,52,54,63,64,76,77] have contributed greatly to the development of new quantum circuit based methodologies to compute the electronic structure in small molecular systems on quantum hardware. However, most of these efforts are deeply hindered by the so-called quantum circuit depth problem[25,26,78,79] where the complexity of the quantum circuit, along with the limited fidelity of the quantum gates currently available on state of the art quantum hardware, lead to an enormous increase in error propagation and leads to unstable implementation. This provides a strong upper bound on accuracy, system size and levels of basis functions that can be implemented on currently available quantum hardware.

As shown in **Fig. 1**, application of standard quantum circuit models[80] to treat electronic structure problems leads to a rapid increase in the circuit depth and the number of CNOT gates. This contributes greatly to the accumulated error during quantum propagation. Quantum gate fidelity for CNOT gates is generally of the order of 95%[81] and the improvement of such gate fidelity is an active area of quantum hardware development.[82] This is related to the fact that the CNOT gates require maximally entangling XX($\pi/2$) gates and hence have lower quality performance[81] as compared to small angle XX gates and this aspect contributes to error propagation. As seen in **Fig. 1**, the number of quantum gates, the number of CNOT gates, and circuit depth increase exponentially with system size. This leads to a dramatic increase in the error in quantum propagation thus restricting both size and quality (in terms of basis set sizes that can be routinely used) of performance. Thus, despite the growing set of available quantum hardware platforms, and the accompanying set of complex quantum algorithms, performing accurate, state-of-the-art quantum chemical calculations will remain a significant challenge for the foreseeable future.

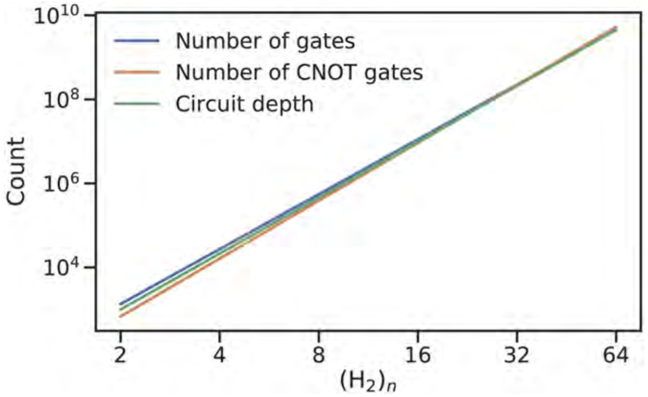

Fig. 1 Quantum circuit depth complexity as a function of system size is illustrated here for a family of $(H_2)_n$-clusters. As system size grows, a standard quantum circuit implementation afforded by the commonly used Qiskit, 80 a quantum software development kit for obtaining and executing quantum circuits on quantum hardware, becomes prohibitively complex. Figure reproduced from Ref. 83.

Given these challenges to quantum computing of molecular electronic structure, this section outlines a hybrid quantum/classical algorithm, based on a graph-theoretic reduction of molecular structure, and is applied towards performing electron correlation calculations on *an ensemble of quantum and classical hardware systems*. The algorithm is a referred to as "Graph-$|Q\rangle\langle C|$" since it contains an independent set of classical and quantum algorithmic components inside one umbrella.[83] To achieve this, in Section 2.1 we introduce a general projection operator formalism that when applied to any complex quantum circuit, in Section 2.2, reduces the circuit into a family of parallel quantum circuits, each of much lower complexity. In the results section we then show that this approach reduces the quantum circuit depth problem shown in **Fig. 1**, by several orders of magnitude. The overall computational workload is partitioned, through graph-theory based on computational complexity analysis, into (a) classical computing sections that are carried out on traditional classical electronic structure packages, such as Gaussian,[84] Psi4,[85] Orca[86] and Quantum Espresso,[87] and (b) quantum computing sections that are carried out using the quantum circuit models. Furthermore, the Graph-$|Q\rangle\langle C|$ algorithm is quantum hardware agnostic and is developed with the goal to be implemented on all quantum hardware technologies, and in fact, is designed to be used on an ensemble of such quantum hardware systems for any given calculation. Graph-$|Q\rangle\langle C|$ is complementary to other ideas in the literature[54,60–62,64] that attempt to reduce quantum gate complexity, and reduces the required quantum circuit depth, the number of quantum gates, and the number of CNOT gates (by several orders of magnitude) that contribute to error accumulation. Given this reduction, Graph-$|Q\rangle\langle C|$ improves quantum algorithmic efficiency, provides a new avenue for quantum resource management, and also may reduce the accumulation of errors during electronic structure calculations on quantum hardware.

2.1 A Hilbert Space Decomposition Scheme Using Venn diagrams and Graphical Decomposition

We begin with a Hilbert space decomposition scheme using the set-theoretic inclusion-exclusion principle.[88] The projection technique is then adapted to a graph problem, which in the next subsection is used to decompose any arbitrary unitary operator (or quantum circuit) into parallel, but overlapping, streams of computing processes that can be executed on a cluster of quantum and classical hardware systems.

Let us begin with a Venn diagram that divides a coordinate representation $|x\rangle\langle x|$ into regions, A, B, C, etc. The regions may intersect and in **Fig. 2**(a), for concreteness, we have superimposed the Venn-diagram on top of a H_2 molecular cluster. Thus, the Venn diagram divides a molecular system into several regions. Using the principle of inclusion exclusion,[88] the resolution of the identity for the Hilbert space depicted within the Venn diagram may be written as

$$\begin{aligned} I \equiv & \int\limits_{A\cup B\cup C} dx|x\rangle\langle x| = \int\limits_{A} dx|x\rangle\langle x| + \int\limits_{B} dx|x\rangle\langle x| + \int\limits_{C} dx|x\rangle\langle x| - \\ & \int\limits_{A\cap B} dx|x\rangle\langle x| - \int\limits_{A\cap C} dx|x\rangle\langle x| - \int\limits_{B\cap C} dx|x\rangle\langle x| + \int\limits_{A\cap B\cap C} dx|x\rangle\langle x| \\ & = \mathcal{P}_A + \mathcal{P}_B + \mathcal{P}_C - \mathcal{P}_{A\cap B} - \mathcal{P}_{A\cap C} - \mathcal{P}_{B\cap C} + \mathcal{P}_{A\cap B\cap C} \end{aligned} \tag{1}$$

where the left side is the identity since it sums over the entire Hilbert space represented here by sets A, B, and C, and integrals involving the dyadic terms, $|x\rangle\langle x|$, are within a chosen set depicted within the Venn diagram. Additionally, we have also introduced projection operators, that project out portions of a Hilbert space depicted in Eq. (1) and only include the portion of the diadic sum within a given set.

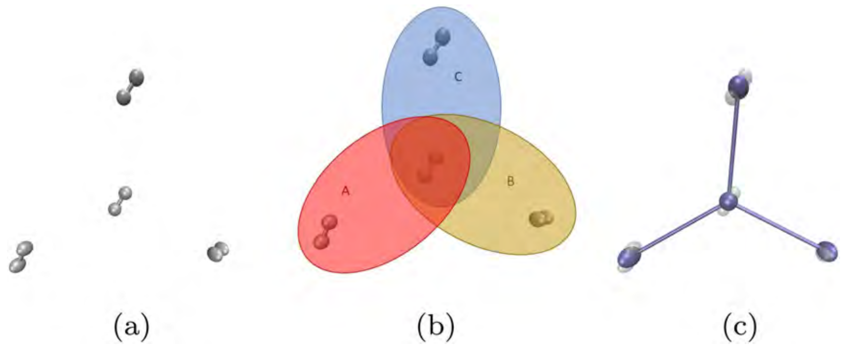

Fig. 2 In Figure (b), we provide an illustration of the sets *A*, *B* and *C* for the system in Figure (a). Figure (b) is used to construct Eq. (1). In Figure (c) the sets provide a graph-theoretic form to make the transition from Eq. (1) to Eq. (4) clear. Figure (c) can be realized through Eq. (6) which is a special case of Eq. (4).

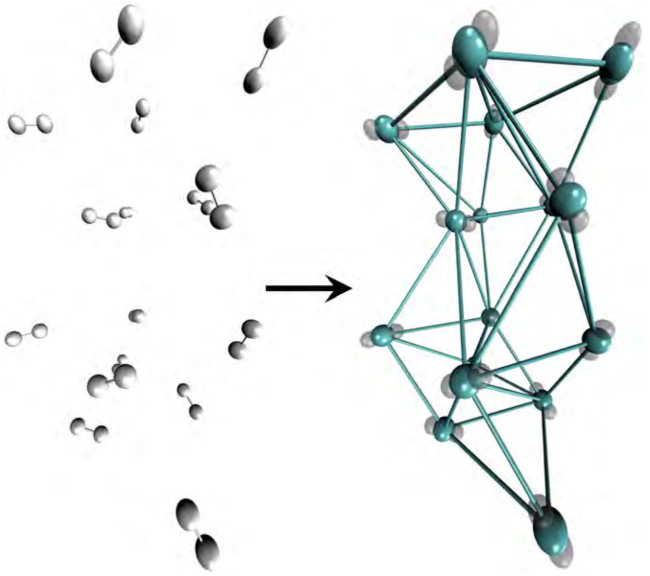

Fig. 3 Here, a cluster of 16 hydrogen molecules is represented as a graph. This graph presents a distance based truncation of expensive electron correlation treatments. This graphical representation also allows for the reduction in complexity for the quantum circuit representation of the systems discussed later in this paper.

$$\mathcal{P}_A \equiv \int_A dx |x\rangle\langle x| \tag{2}$$

While Eq. (1) arises from the principle of inclusion exclusion[88] well-known in set-theory, and can be generalized to an arbitrary number of sets, an alternate approach to divide the molecular space represented by the identity operator, I, can be obtained by introducing a graph decomposition of molecular structure. To begin with, the molecular assembly, similar to that in **Fig. 1**, is partitioned into a set of nodes, or vertices. These nodes may be determined on a chemical basis or numerical basis, and first-order interactions between these discrete nodes are captured by creating edges, that are the union of a pair of nodes. Once the nodes and edges are defined, the chemical system of interest is now represented as a graph (An illustration of our graph-theoretic partitioning of molecular structure is presented in **Fig. 3**).

In our discussion below, the set of nodes described above is represented as V_0. Similarly, the family of edges that represent all first-order interactions between nodes are represented as V_1. Together these nodes and edges define a graph, $\mathcal{G} \equiv \{\mathrm{V}_0; \mathrm{V}_1\}$ (see **Fig. 3**). The graph, thus, comprises nodes, V_0, edges, V_1 and rank-r objects, known as simplexes[89–91] (Simplexes are defined as geometric objects with an arbitrary number of vertices, where all pairs of vertices are connected[89–91]). The set of such rank-r objects is represented as V_r:

$$\{\mathrm{V}_r \mid r = 0, 1, 2, \cdots\} \equiv \{\mathrm{V}_0, \mathrm{V}_1, \mathrm{V}_2, \cdots\}. \tag{3}$$

and these capture all needed higher-order interactions between the nodes.

An equivalent expression for the resolution of the identity in Eq. (1), may now be obtained in terms of projectors that encompass nodes, edges, and higher order simplexes as

$$\begin{aligned} \mathrm{I} = & \sum_{\alpha\in \mathrm{V}_0} \mathcal{M}_\alpha^0 \mathcal{P}_{\alpha,0} - \sum_{\alpha\in \mathrm{V}_1} \mathcal{M}_\alpha^1 \mathcal{P}_{\alpha,1} + \\ & \sum_{\alpha\in \mathrm{V}_2} \mathcal{M}_\alpha^2 \mathcal{P}_{\alpha,2} - \cdots \\ = & \sum_{r=0}^{\mathcal{R}} (-1)^r \sum_{\alpha\in \mathrm{V}_r} \mathcal{M}_\alpha^r \mathcal{P}_{\alpha,r} \end{aligned} \tag{4}$$

Here, $\mathcal{M}_\alpha^r \equiv \left[\sum_{m=r}^{R} (-1)^m p_\alpha^{r,m}\right]$ and $p_\alpha^{r,m}$ are the number of times the α^{th} rank-r term (in set V_r) appears in all rank-m terms (in set V_m), for $m \geq r$. Consequently M_α^r is the overcounting correction for the number of times the α^{th} rank-r term appears in all objects of rank greater than or equal to r. It must be noted that $p_\alpha^{r,m}$ are also the number of supersets of the α^{th} rank-r simplex, and the projectors, $\mathcal{P}_{\alpha,r}$, yield the α-th rank-r simplex.

The parallels between Eq. (4) and Eq. (1) may be further explored by rewriting Eq. (4) in decreasing order of rank, that is,

$$\mathrm{I} = (-1)^{\mathcal{R}} \left\{ \sum_{\alpha\in \mathrm{V}_{\mathcal{R}}} \mathcal{P}_{\alpha,\mathcal{R}} - \sum_{\alpha\in \mathrm{V}_{\mathcal{R}-1}} \mathcal{M}_\alpha^{\mathcal{R}-1} \mathcal{P}_{\alpha,\mathcal{R}-1} + \sum_{\alpha\in \mathrm{V}_{\mathcal{R}-2}} \mathcal{M}_\alpha^{\mathcal{R}-2} \mathcal{P}_{\alpha,\mathcal{R}-2} - \sum_{\alpha\in \mathrm{V}_{\mathcal{R}-3}} \mathcal{M}_\alpha^{\mathcal{R}-3} \mathcal{P}_{\alpha,\mathcal{R}-3} + \cdots \right\} \tag{5}$$

where the appearance of alternating signs is clear and resembles that in Eq. (1), and the factor, $\mathcal{M}_\alpha^{R-1}$ is the number of times the α-th rank-$(\mathcal{R}-1)$ simplex appears in all rank-$\mathcal{R}$ simplexes. Additionally, for $\mathcal{R} = 1$, Eq. (5) becomes

$$\mathrm{I} = -\sum_{\alpha\in \mathrm{V}_1} \mathcal{P}_{\alpha,1} + \sum_{\alpha\in \mathrm{V}_0} \mathcal{M}_\alpha^0 \mathcal{P}_{\alpha,0} \tag{6}$$

which, for the graph in **Fig. 2**(c), leads to an identical result as in Eq. (1), constructed for **Fig. 2**(b).

2.2 Quantum Circuit Depth Reduction Through Parallel Quantum Processing Using the Projection Operators, $\{\mathcal{P}_{\alpha,r}\}$

We now begin with a quantum circuit depicted using the symbol, $\mathcal{U}$, a unitary operator, that propagates a state that represents the electronic structure for the full molecular system on some quantum hardware system. However, as noted in **Fig. 1**, the complexity of such a circuit and the associated resources may grow rapidly as system size grows. To overcome this issue, we may apply the graph-theoretically defined resolution of identity in Eq. (4) to $\mathcal{U}$ to decompose it into a family of parallel quantum circuits given by

$$\begin{aligned} \mathrm{I}\ \mathcal{U} &= \sum_{r=0}^{\mathcal{R}} (-1)^r \sum_{\alpha\in \mathrm{V}_r} \mathcal{M}_\alpha^r \left[\mathcal{P}_{\alpha,r}\ \mathcal{U}\right] \\ &= \sum_{r=0}^{\mathcal{R}} (-1)^r \sum_{\alpha\in \mathrm{V}_r} \mathcal{M}_\alpha^r\ \mathcal{U}_{\alpha,r} \end{aligned} \tag{7}$$

where

$$\left\{\mathcal{U}_{\alpha,r} \equiv \mathcal{P}_{\alpha,r}\ \mathcal{U}\right\} \tag{8}$$

represent here a set of projected quantum circuits, one for each simplex. When a molecular system is divided using the graph, the set $\{\mathcal{U}_{\alpha,r}\}$ yields one quantum circuit for each molecular fragment. This is illustrated in **Fig. 4**.

2.3 Many-Body Expansions From the Quantum Circuit Decomposition

We use the individual quantum circuits, $\{\mathcal{U}_{\alpha,r}\}$, to obtain a family of fragment energies $\left\{E_{\alpha,r}^{UCCSD}\right\}$, using quantum circuit models using the Unitary Coupled Cluster Singles and Doubles (UCCSD) approach,[83] that when used in Eq. (7), yields

$$E_{|Q\rangle\langle C|}^{MBE-UCCSD} = \sum_{r=0}^{\mathcal{R}} (-1)^r \sum_{\alpha\in \mathrm{V}_r} E_{\alpha,r}^{UCCSD} \mathcal{M}_\alpha^r \tag{9}$$

Eq. (9) yields a stream of parallel quantum processes. This idea is presented in **Fig. 4**. Since these independent circuits, $\{\mathcal{U}_{\alpha,r}\}$, are for much smaller fragments as compared to the full system of interest, one may find the error propagation to be limited. We indeed show this to be the case for the examples discussed later.

2.4 Improving the Accuracy of the Quantum-MBE Through Extrapolation

The above graphical description allows a dynamic and flexible representation of local many-body interactions. We now discuss a composite energy measure that has been shown to converge faster as a function of maximum rank-$\mathcal{R}$[92,93] for ground state post-Hartree-Fock energies, AIMD trajectories and multi-dimensional potential calculations using post-Hartree-Fock energies and gradients. The energetic measure we begin with,[92–102] is a composite expression[103–107] and consists of a perturbative, ONIOM-type,[108] correction to a result obtained at a lower level of theory, where the perturbative correction is the difference between two many body expansions (replacing the

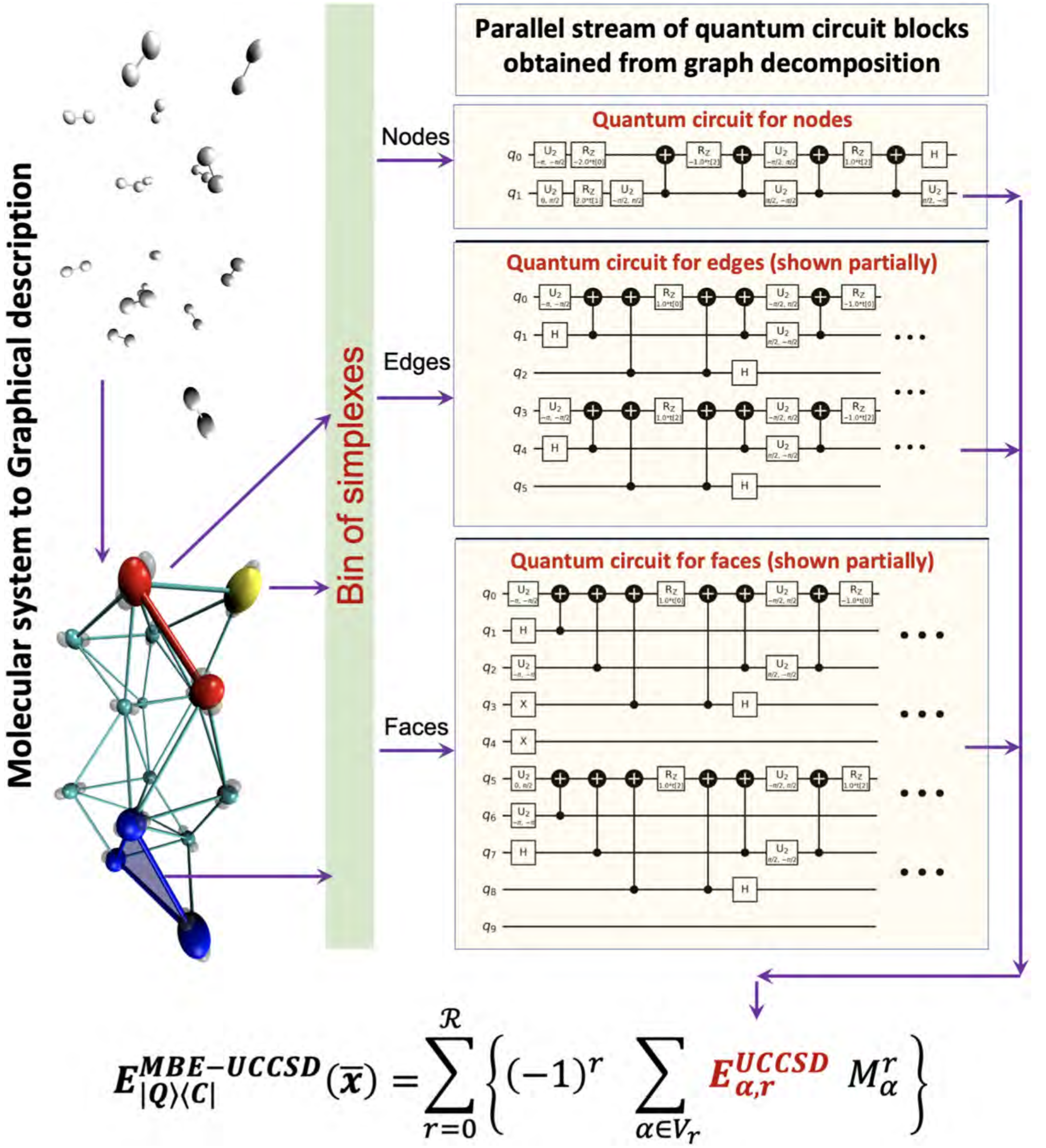

Fig. 4 Implementing Eq. (9) on quantum hardware using the graph partitioning approach. The second-quantized Hamiltonians for node/edge/face fragments, with molecular orbitals obtained from Hartree-Fock, are used as the input for Qiskit,[80] to obtain the quantum circuits shown on the right side of the figure, one circuit for each fragment. Figure reproduced from Ref. 83.

standard "model-high" minus "model-low" portion in ONIOM) given by the graphical representation above. Thus,

$$E^{extrap-UCCSD}_{|Q\rangle\langle C|}(\bar{x}) = E^{DFT}(\bar{x}) + E^{MBE-UCCSD}_{|Q\rangle\langle C|}(\bar{x}) - E^{DFT}_{MBE}(\bar{x}) \tag{10}$$

where the left side, $E^{extrap-UCCSD}_{|Q\rangle\langle C|}(\bar{x})$, denotes the graph-theoretically obtained many-body extrapolation to UCCSD, and the term $E^{MBE-UCCSD}_{|Q\rangle\langle C|}(\bar{x})$ on the right side incorporates the value from Eq. (9) at geometry $\bar{x}$. The quantity, $E^{DFT}_{MBE}(\bar{x})$ is a similar expression computed classically that is,

$$E^{DFT}_{MBE} = \sum_{r=0}^{\mathcal{R}} (-1)^r \sum_{\alpha\in V_r} E^{DFT}_{\alpha,r} \mathcal{M}^r_\alpha \tag{11}$$

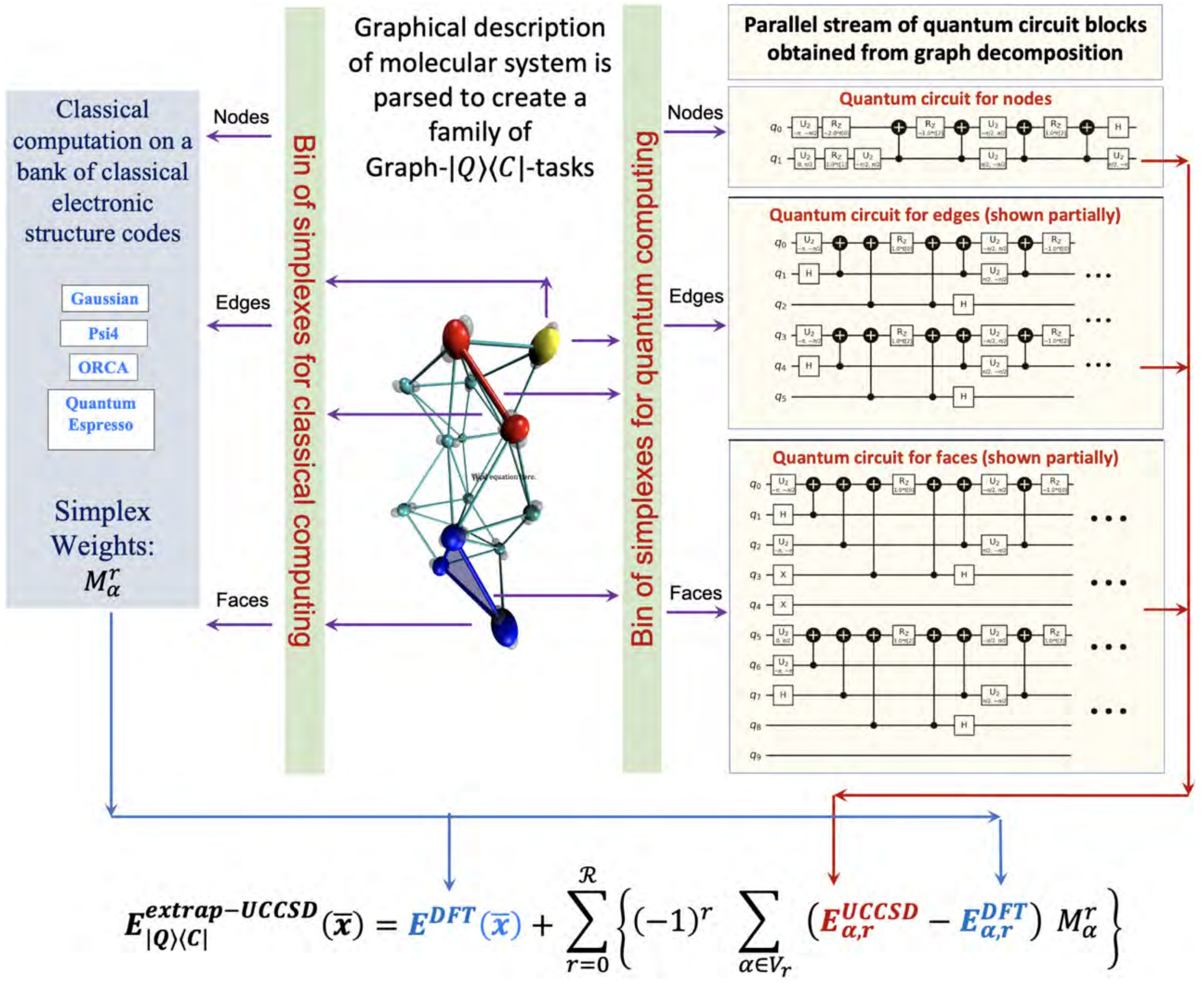

Fig. 5 Fig. 4 presents a quantum circuit decomposition based on graphical partitioning of molecular systems. This helps compute $\left\{E^{UCCSD}_{\alpha,r}\right\}$. To compute the lower scaling $\left\{E^{DFT}_{\alpha,r}; E^{DFT}\right\}$, we use classical computing algorithms as seen on the left side of the figure here.

Thus, the algorithm here envisions spawning out a family of processes on an ensemble of classical and quantum systems, and this process is depicted in Fig. 5, and in more detail, in Fig. 6. The resultant final energy expression in Eq. (10), while presented here for quantum-computing applications, is closely related to multiple ONIOM-based,[108–114] molecular fragmentation methods[107,114–128] as well as developments in many-body theory.[118,119,129–138]. Eqs. (9), (10) and (11) have been actively benchmarked for classical computing studies on AIMD and for potential energy surfaces for gas-phase and condensed phase systems,[92–101] and also provide novel approaches to reduce the complexity of the training cycle in machine learning treatments.[139]

2.5 Computational Aspects

As stated in Fig. 5, the quantity $E^{DFT}_{\alpha,r}$ is computed on classical hardware systems, whereas, the quantity $E^{UCCSD}_{\alpha,r}$, is to be computed on quantum hardware using the quantum circuits $\mathcal{U}_{\alpha,r}$, as facilitated by the graph-theoretic partitioning method.

Fig. 5 provides a brief overview of the algorithm which is further elaborated upon in Fig. 6. Specifically, once the graph is defined, based on its connectivity and the value of $\mathcal{R}$, a range of constituent molecular fragments are obtained, each labeled using the pair of symbols, (α, r), in Eq. (7); these fragments may be pre-determined on classical hardware for relatively small values of $\mathcal{R}$. The process of defining a graph itself is controlled by two parameters, the maximum edge length cutoff which is determined based on the physical range of interactions to be captured, and the maximum order (or rank) of the many body terms which is represented using the symbol $\mathcal{R}$. As the maximum edge length increases, the fragments grow in number and size rapidly, thus increasing computational complexity while also presenting a significant challenge for parallel processing. Edge length cutoff may be chosen to be high enough to include all critical interactions.

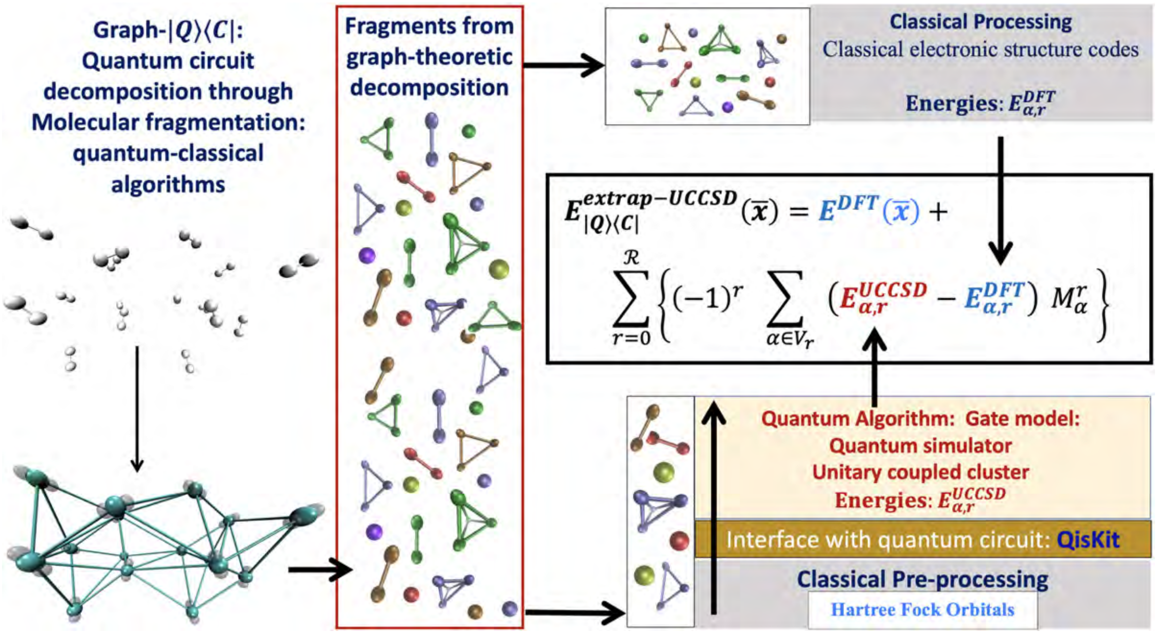

Fig. 6 The algorithm has classical as well as quantum counterparts. Also see **Fig. 5**.

Once the graph is generated the system is decomposed into a set of fragments, that can be processed in an asynchronous manner. A stream of fragments is thus generated with the goal to compute $\left\{E^{UCCSD}(\alpha, r); E^{DFT}(\alpha, r)\right\}$ and E^{DFT} for the full system. In Refs. 92,93, this is done through an MPI parallelized hybrid C++/Python module. The implementation of the approach on classical computing platforms currently supports the following set of external electronic structure packages during a single energy and gradient evaluation: Gaussian,[84] ORCA,[86] and Psi4,[85] for molecular and cluster calculations, and Quantum Espresso,[87] and OpenMX[140] for condensed phase studies. In Ref. 93 this aspect is further expanded to also include the use of quantum algorithms to determine, E^{UCCSD}. (See **Figs. 5** and **6**.).

While our approach will address all of these challenges, by reducing the needed circuit depth, in this publication we discuss the principle behind our execution model for accuracy purposes. Furthermore, as we will see later, it is straightforward to integrate the current scheme into other circuit optimization techniques,[141,142] to further increase the size of systems that can be studied, and this will be considered as part of future publications.

The following steps are used to obtain $\left\{E^{UCCSD}_{\alpha,r}\right\}$ with quantum algorithms

1. Hartree-Fock orbitals for each molecular fragment are classically pre-computed to create a family of second-quantized Fermionic Hamiltonians, and these are together provided as input to the Qiskit quantum computing framework,[80] as shown on the bottom right portion of **Fig. 6**.
2. The family of fragmented second-quantized Fermionic Hamiltonians are then converted into quantum circuits, $\{\mathcal{U}_{\alpha,r}\}$, using a parity mapping protocol.[143]
3. Each fragment quantum circuit is then executed on Qiskit's built-in statevector simulator without using a noise model, and the resultant energies are optimized using the SLSQP optimizer[144] available within VQE.[51] This yields the family of UCCSD energies, $\left\{E^{UCCSD}(\alpha, r)\right\}$ used to obtain the molecular energy as per Eqs. (9), (10) and (11).

The hybrid quantum/classical formalism developed here is transparent to the underlying quantum mapping protocol used to convert the Fermionic Hamiltonians for each individual molecular fragment into quantum circuits. Thus there are no restrictions on the kind of map used to treat each individual fragment Hamiltonian, and in principle we can use the Jordan-Wigner,[73] Bravyi-Kitaev[75] or parity mapping[143] transformations. Here, we have tested the Jordan-Wigner scheme as well as parity mapping protocol, and we find that the latter does in fact reduces the qubit resources needed as suggested in Ref. 143. Specifically, for each quantum circuit, two qubits are reduced with the spin-parity symmetries of the system,[143] as a separate optimization technique.

2.6 Generality of the Graph-$|Q\rangle\langle C|$ Algorithm

It is critical to emphasize at this stage that it is now accepted[25,26] that universal, fully fault-tolerant, quantum computers are a rather distant dream,[25] and new frontiers such as Noisy Intermediate Scale Quantum (NISQ)[25] systems have emerged. To effectively use such NISQ machines with their limited coherence times, a hybrid approach that interleaves NISQ machines with classical computers has been proposed in Ref. 26. This is complemented by orthogonal developments in quantum chemical algorithm developments where the variational quantum eigensolver (VQE)[63,64] is already known to be a hybrid quantum-classical approach. In this regard, our approach here, containing quantum and classical algorithmic components, is a contribution that can be used for ground state quantum chemical calculations at enhanced accuracy with lower computational complexity[92,93,96–98] on a hybrid stream of quantum and classical systems. The algorithm is built to be asynchronous and parallel, and these computational aspects will be considered in a future publication.

Furthermore, there have been several recent studies that allow the implementation of variational quantum algorithms such as the Variational Quantum Eigensolver (VQE),[43,44,51,52,54,145] in combination with an appropriate trial wavefunction such as the Unitary Coupled Cluster (UCC) ansatz[146,147] on quantum simulation systems. The approach discussed here is general enough to allow the possibility to include other eigensolvers apart from VQE, such as the recently developed contracted quantum eigensolver (CQE)[77] to compute the set of $\{E^{UCCSD}(\alpha, r)\}$ values from the associated two-particle reduced density matrices.

3 Quantum Computing Methods for Quantum Molecular Dynamics and Spectroscopy

The implementation of multi-dimensional molecular dynamics studies on quantum hardware is complicated by multiple factors. Molecules contain many correlated nuclear degrees of freedom, and each of these correlated nuclear degrees of freedom needs to be represented in some discretized basis. If we assume $\mathcal{N}$ discretizations (or basis vectors) per nuclear degree of freedom and N nuclear degrees of freedom, the complexity of information grows approximately as $\mathcal{N}^N$. This includes both the effort involved in computing potential energy surfaces using accurate post-Hartree Fock methods, such as those discussed in the previous section, and also computing the quantum nuclear propagation. As a result, quantum nuclear dynamics is thought to be an exponentially hard problem.

In contrast to the many electronic structure algorithms currently being developed[43–59] for implementation on quantum hardware, the intrinsic spin statistics of quantum nuclear dynamics problems, arising for the nuclear permutation symmetries do not have a role under conditions prevalent in biological, materials, and atmospheric systems, such as hydrogen transfer reactions under ambient conditions. As a result, most such quantum dynamics studies are currently constructed on classical computing platforms using basis sets and on grids. Furthermore, many of these problems are known to display anomalous nuclear quantum effects[9,148,149] that are challenging to study on classical hardware due to the exponentially scaling computational cost of quantum dynamics with increasing degrees of freedom. Unlike several recent attempts on the electron correlation problem,[43–59] approximating quantum nuclear dynamics problems on quantum computing platforms has received relatively less attention.[65–71]

This section shows a mapping protocol that allows the study of quantum nuclear dynamics problems on quantum hardware that do not require knowledge of the spin statistics obeyed by the constituent systems. We discuss an approximate algorithm to map exponentially-scaling quantum nuclear dynamics problems on a single Born-Oppenheimer surface, onto a general class of Ising-model Hamiltonians. Such Ising-type Hamiltonians may be implemented on a range of quantum computing platforms, such as ion-traps,[27,28,150–152] super-conducting coils,[31] Bosonic processors with photons,[33–35] solid state devices and quantum dots inside cavities,[36–39] and Rydberg atoms.[40,42]

The most significant features of the mapping algorithm are summarized in **Fig. 7**, with a more detailed illustration provided in **Fig. 8**. An example of a quantum nuclear problem is shown in **Fig. 8**a and also on the left side of **Fig. 7**. Here we depict a system containing a short-strong hydrogen bond with anharmonic vibrational behavior along the donor-acceptor axis. This problem is prototypical and is representative of a broad range of systems that occur during hydrogen transfer reactions[148] and in hydrogen-bonded systems that are known to have significance in many critical processes.[153] We pre-compute the Born-Oppenheimer potential using electronic structure calculations, perhaps in future using the techniques from the previous section, and obtain a discrete version of the quantum nuclear Hamiltonian. To map this Hamiltonian onto a spin-lattice Ising-type model, the key insights in this paper are as follows: (1) A projected subspace of a specific unitary

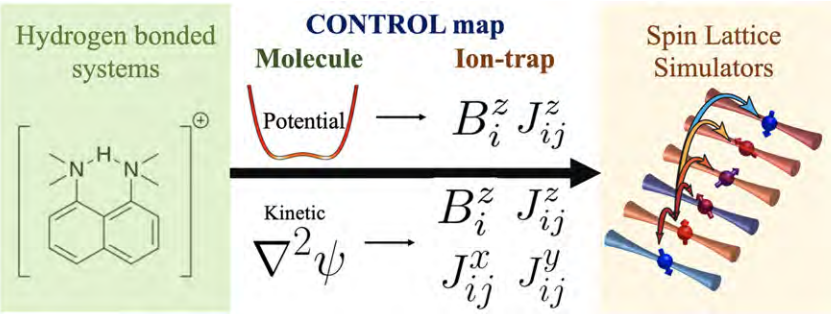

Fig. 7 Figure outlines the critical features of our mapping algorithm. The Born-Oppenheimer potential as well as kinetic energy portions of the molecular Hamiltonian are mapped to control parameters, $\left\{\{B_i^z\}; \{J_{ij}^x, J_{ij}^y, J_{ij}^z\}\right\}$, of a Ising-type spin-lattice simulator.

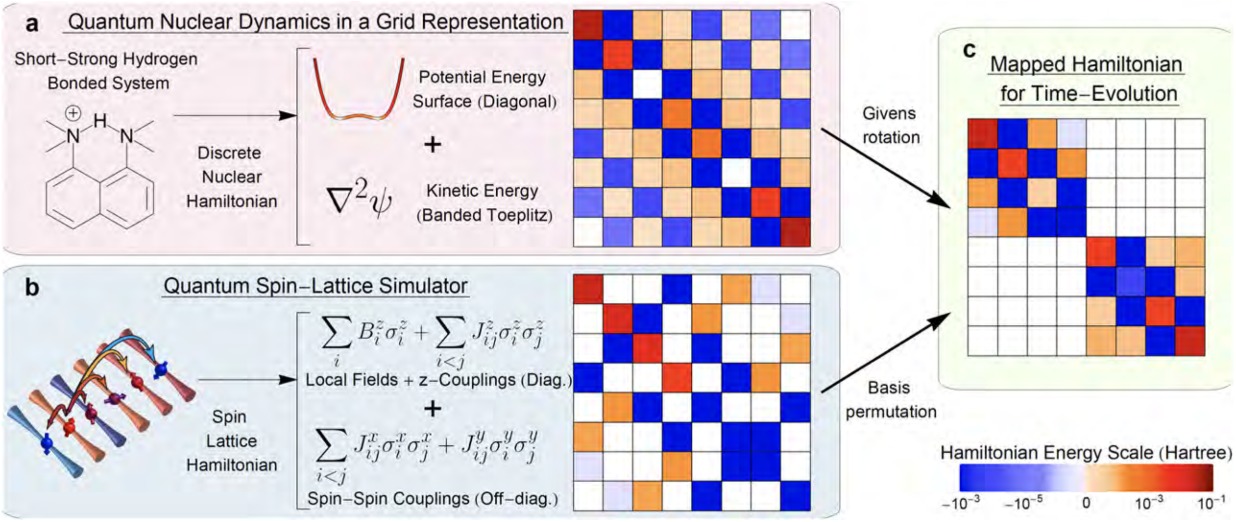

Fig. 8 The algorithm converts the Born-Oppenheimer potential surface and kinetic energy terms in a quantum-nuclear problem to a set of controllable parameters and facilitates the dynamical evolution of quantum states in an ion-trap. Box (a) shows the Born-Oppenheimer potential and kinetic energies for a short-strong hydrogen bonded system. This system Hamiltonian is mapped onto an ion trap quantum simulator shown in box (b). Discrete representation of the nuclear Hamiltonian and appropriate rotations yield ion-trap parameters, $\{\{B_i^z\};\{J_{ij}^x, J_{ij}^y, J_{ij}^z\}\}$, to determine the Ising model used to control the dynamics of lattice spin-states. Also see Fig. 7.

transformation of the diagonal elements of the quantum nuclear Hamiltonian (related to the Born-Oppenheimer potential) maps to and defines the local magnetic fields applied on each lattice site of an Ising model Hamiltonian. (2) A similarly projected subspace of a related unitary transformation of the off-diagonal elements of the quantum nuclear Hamiltonian (related to the nuclear kinetic energy operator) defines and is mapped onto the inter-site coupling terms in the Ising model. These features of our map are highlighted in Fig. 7.

Importantly, this approach is different from the standard circuit model,[154] and here, the matrix elements of the nuclear Hamiltonian that describe the molecular dynamics, inform the choice of local magnetic fields applied on each physical qubit (or lattice) site and laser pulse intensities that dictate the inter-site coupling, and govern the dynamics of the ion-trap quantum platform.

This Section is organized as follows: In Section 3.2, we inspect the block structure of the Ising Hamiltonian which informs the general class of problems that may be computable on hardware architectures used to realize such Ising-type Hamiltonians. Following this, we then introduce the quantum nuclear Hamiltonian matrix on a single Born-Oppenheimer surface in Section 3.3 and a class of Givens rotations[155] based matrix transformations in Section 3.4 to represent the quantum nuclear Hamiltonian matrix in a form that is commensurate with the transformed form of the Ising model Hamiltonian in Section 3.2 This transformation leads to our approximate mapping protocol that is outlined in Section 3.5. Numerical results for the anharmonic molecular vibrations of the shared proton in a symmetric short-strong hydrogen bonded system are provided in Section 5. These include explicit numerical propagation of both the molecular dynamics problem as well as the spin lattice dynamics governed by Ising-type Hamiltonian where the Ising Hamiltonian parameters are chosen based on the mapping protocol in Section 3.5. The results match exactly for the case of three-qubits and error estimates beyond three-qubits discussed in Ref. 72.

3.1 The Generalized Ising-Like Hamiltonian Programmable on a Variety of Quantum Devices

Ising-type Hamiltonians can be implemented on a range of available quantum computing platforms,[27,28,31,33,40–42] which makes these one of the most commonly-used quantum computing models today.[28,156] However, for specificity, we will illustrate our mapping protocols for ion-trap based quantum architectures, where ions form defect-free arrangements and can support quantum coherence times longer than 10 min.[157] Interactions between ions map to interactions between effective quantum spin states and quantum-harmonic-oscillator bath states – each of which can be precisely controlled and programmed using laser light.[158] Site-resolved detection of each ion's spin state can be achieved with near-unit fidelity.[159] These features have made trapped ions the leading platform for establishing atomic frequency standards[160] and one of the leading candidates for performing quantum simulations and quantum computations on such interacting spin systems.[28,161–166]

For ion-trap quantum hardware, the generalized Ising Hamiltonian is represented by a spin-lattice of qubits, where (1) the energy gap between the states at each qubit, i, and their relative orientations, are controlled by local effective magnetic fields, $\{B_i^x, B_i^y, B_i^z\}$, and (2) the spin-spin coupling between different lattice sites, i and j, is controlled using laser pulses, also spatially non-isotropic, and represented as $\left\{J_{ij}^x, J_{ij}^y, J_{ij}^z\right\}$. Thus, the most general Hamiltonian achievable within the ion trap quantum hardware at low temperatures is

$$\begin{aligned}\mathcal{H}_{IT} = &\sum_{i=1}^{N-1}\sum_{j>i}^{N}\left\{J_{ij}^x\sigma_i^x\sigma_j^x + J_{ij}^y\sigma_i^y\sigma_j^y + J_{ij}^z\sigma_i^z\sigma_j^z\right\} \\ &+ \sum_{i=1}^{N}\left\{B_i^x\sigma_i^x + B_i^y\sigma_i^y + B_i^z\sigma_i^z\right\}\end{aligned} \tag{12}$$

where N is the number of qubits (or ion-sites). The quantities σ_i^x, σ_i^y, and σ_i^z are the Pauli spin operators along the respective directions of the Bloch sphere on the i-th lattice site. It is critical to note that the expression above is more general than that commonly used in condensed matter physics and quantum chemistry, where only nearest neighbor interactions are considered. In fact, the set of programmable Ising-type Hamiltonians on an ion trap quantum computer depicts a complete graph that connects all qubits in a spin-lattice system with programmable interactions.[167]

In Ref. 72, we map the Born-Oppenheimer nuclear Hamiltonian to Eq. (12), thus allowing the two quantum systems to undergo analogous quantum dynamics. Towards this, the parameters $\{B_i^\gamma; J_{ij}^\gamma\}$ are "programmed" as per the elements of the classically determined Born-Oppenheimer nuclear Hamiltonian matrix. To arrive at such a map, we first examine the intrinsic symmetries that are present within such generalized Ising Hamiltonians.

3.2 Block Structure of Ising-Type Hamiltonian Matrices Obtained From Appropriate Classification of the Computational Basis

The ion-trap Hamiltonian, $\mathcal{H}_{IT}$, is naturally represented in a basis of 2^N spin states, where for example, $\{|\uparrow\uparrow\rangle, |\uparrow\downarrow\rangle, |\downarrow\uparrow\rangle, |\downarrow\downarrow\rangle\}$ form a basis for a 2-qubit system. These now provide us with a "computational basis" with programmable handles, $\{B_i^\gamma; J_{ij}^\gamma\}$. We find that

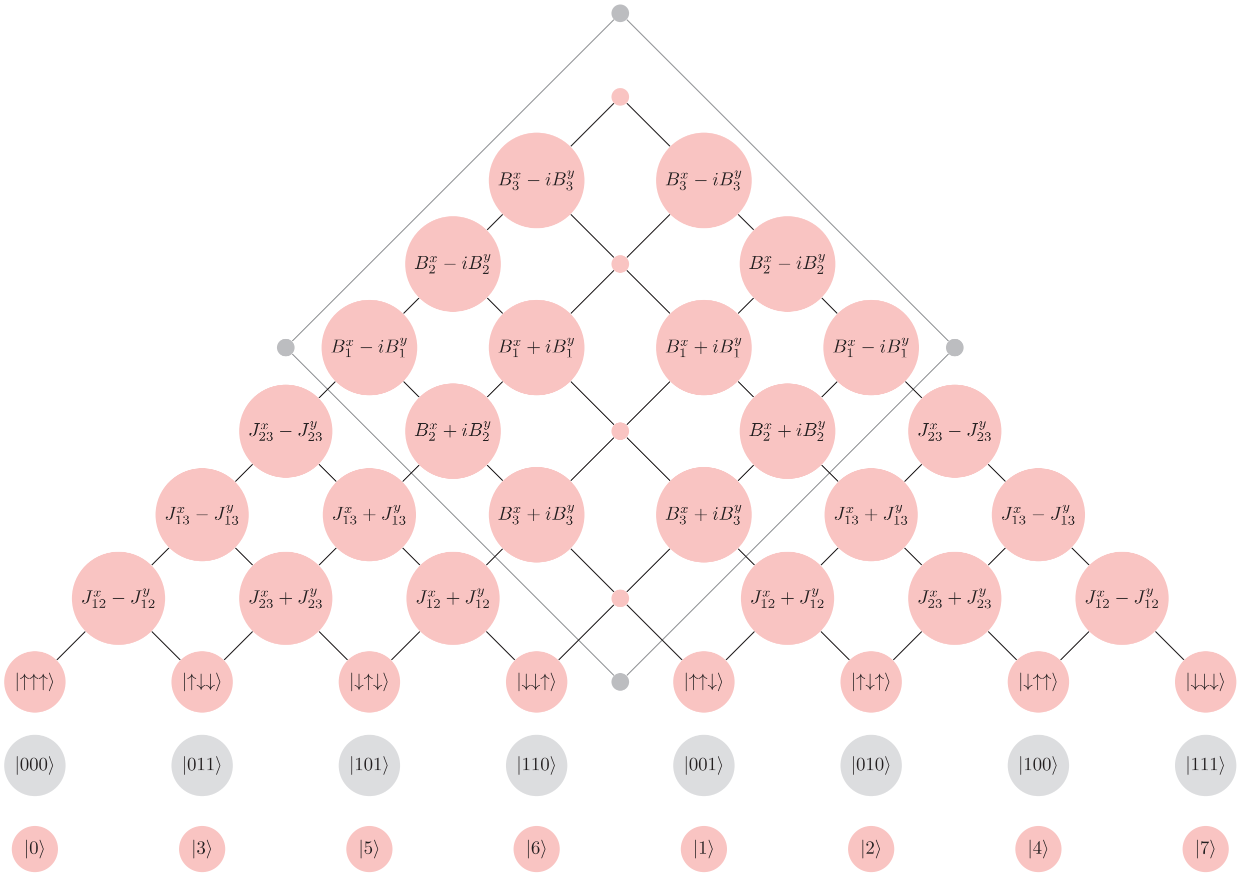

Fig. 9 The upper triangular part (excluding the diagonal) of the Ising Hamiltonian, $\mathcal{H}_{IT}$ (Eq. (12)), in the permuted computational basis is illustrated for a three qubit system. Spin (computational) basis state kets, along with their corresponding binary and integer representations, are presented at the base of the figure. These states are partitioned into odd, and even spans of the total spin raising operators. The interaction between any two states, $|i\rangle$ and $|j\rangle$ is the ij^{th} matrix element of the ion trap Hamiltonian. For example, $\langle\uparrow\downarrow\uparrow|\mathcal{H}_{IT}|\downarrow\downarrow\downarrow\rangle \equiv \left[J_{13}^x - J_{13}^y\right]$. The off-diagonal block that couples the vectors obtained from the odd, and even spans of the total spin raising operators are marked using a gray square.

a general set of permutations on the computational basis vectors to reveal a novel block structure of the Ising Hamiltonian matrix. Specifically, the 2^N spin states are partitioned into two sets that are created by the span of even and odd total spin raising operators. See the set of vectors in the bottom left row of **Fig. 9**, where this idea is illustrated for a three-qubit system. For the notation in this paper, we have used the binary representation, $|11\cdots\rangle$ for spin state, $|\downarrow\downarrow\cdots\rangle$ and the corresponding integer representation $|2^N-1\rangle\rangle$ obtained from the bit-sequence encoded in $|11\cdots\rangle$.

When the spin basis vectors are partitioned in this fashion, the Ising Hamiltonian in Eq. (12) separates into the block structure that is illustrated in **Fig. 9** for a three-qubit system. Specifically, the matrix that determines the time-evolution of the hardware system separates into two diagonal blocks that can only be coupled by turning on $\left\{B_i^x; B_i^y\right\}$ and this is shown in **Fig. 9** as part of the gray square. Thus eliminating these $\left\{B_i^x; B_i^y\right\}$ fields would yield two separate diagonal blocks allowing the treatment of systems that may have a similar block structure. Similarly, the off-diagonal matrix elements within each diagonal block are determined by the laser field parameters, $\left\{J_{ij}^x; J_{ij}^y\right\}$. While the structure derived here is completely general, it is illustrated in **Fig. 9** for a 3-qubit system. The diagonal elements of the matrix, not shown in **Fig. 9** to maintain clarity, contain linear combinations of $\{B_i^z; J_{ij}^z\}$.

For larger number of qubits, the block structure has a recursive form. This block-form of the Ising-type Hamiltonian and the associated structure in **Fig. 9**, is a significant general result[72]. To the best of our knowledge such a structure of the general Ising model has never been discussed in the literature, and as we find below, this analysis is critical towards mapping arbitrary problems.

3.3 The Grid Based Quantum Nuclear Hamiltonian Computed on Classical Hardware

In the coordinate representation with basis elements, $\{|x\rangle\}$, the quantum nuclear Hamiltonian matrix elements are given by,

$$\langle x|\mathcal{H}^{Mol}|x'\rangle = K(x,x') + \mathrm{V}(x)\delta\left(x-x'\right) \tag{13}$$

For local potentials, the potential energy operator, $\hat{\mathrm{V}}$, is diagonal in the coordinate representation. The expression in Eq. (13) yields a continuous representation, and in practice the matrix and the corresponding vectors that the matrix acts on are represented on a discretized Cartesian grid. The potential energy in the above equation is obtained from electronic structure calculations, that may be performed on quantum hardware, perhaps using the algorithm used above.

We employ an analytic banded Toeplitz distributed approximating functional (DAF)[168,169] representation for the grid representation of the kinetic energy operator in Eq. (13):

$$\begin{aligned} K(x,x') = K(|x-x'|) = \frac{-\hbar^2}{4m\sigma^3\sqrt{2\pi}}\exp\left\{-\frac{x-x'\ ^{2}}{2\sigma^2}\right\} \\ \sum_{n=0}^{M_{DAF}/2} \ \frac{-1}{4}\ ^{n}\frac{1}{n!}H_{2n+2}\ \frac{x-x'}{\sqrt{2}\sigma}\ . \end{aligned} \tag{14}$$

The banded-Toeplitz representation of the DAF approximation for the kinetic energy operator, where the property of its matrix elements, $K_{ij} \equiv K(|i-j|)$, has a critical role in reducing the nuclear Hamiltonian to the form of $\mathcal{H}_{IT}$, depicted in **Fig. 9**. In Eq. (14), $H_{2n+2}\left(\frac{x-x'}{\sqrt{2}\sigma}\right)$ are the even order Hermite polynomials that only depend on the spread separating the grid basis vectors, $|x\rangle$ and $|x'\rangle$, and M_{DAF} and σ are parameters that together determine the accuracy and efficiency of the resultant approximate kinetic energy operator.

3.4 Unitary Transformations That Yield the Block Structure of the Nuclear Hamiltonian, for Symmetric Potentials, to Make These Commensurate With and Mappable to the Spin-Lattice Hamiltonian, $\mathcal{H}_{IT}$

The nuclear Hamiltonian, $\mathcal{H}^{Mol}$ from Eq. (13), has a banded Toeplitz structure due to the kinetic energy being expressed in terms of DAFs. In general, the Hamiltonian in Eq. (13) represents a multi-dimensional quantum dynamics problem, where the number of dimensions directly corresponds to the number of nuclear degrees of freedom. Here, we examine the map between the Hamiltonian in Eq. (13) for symmetric one-dimensional potentials and the Ising model Hamiltonian discussed in Section 3.2. Routes from here to unsymmetric potentials and to problems in higher dimensions are discussed in a series of publications being prepared from our group that utilize tensor networks.

The unitary transform that leads to the block structure of the nuclear Hamiltonian, similar to the structure of the Ising Hamiltonian, can be expressed as a product of Givens rotations. The effect of the Givens rotations on the grid basis states is to create superposition states of the symmetric grid basis states. To explain this, we introduce a uniform one-dimensional set of 2^N grid points, $\{|x_i\rangle\}$, such that the Givens transformed grid basis, $\{|\tilde{x}_i\rangle\}$, may be represented as

$$|\tilde{x}_i\rangle \equiv \frac{1}{\sqrt{2}}[|x_i\rangle + |x_{n-i}\rangle], \quad 0 \le i < (n+1)/2 \tag{15}$$

$$|\tilde{x}_i\rangle \equiv \frac{1}{\sqrt{2}}[|x\rangle_i - |x_{n-i}\rangle], \quad (n+1)/2 \le i \le n \tag{16}$$

where $n = 2^N - 1$. The grid basis and the Givens transformed grid basis, for a three-qubit system, are represented on the left

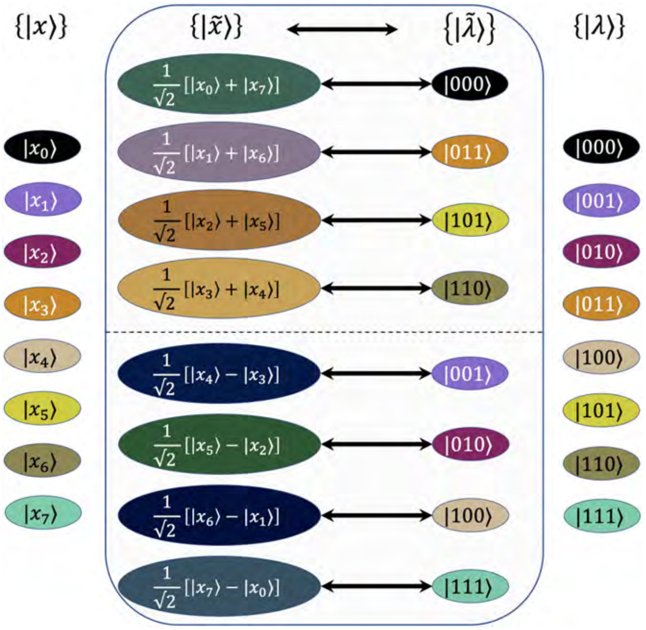

Fig. 10 An illustration of the mapping of the Givens transformed grid basis state representation, $|\tilde{x}\rangle$ (Eq. (16)), for the discrete quantum nuclear Hamiltonian to the permuted computational basis state representation, $|\tilde{\lambda}\rangle$ (Section 3.2), for the Ising model Hamiltonian. The respective basis states map shown here for the case of 3 qubits holds true and can be generalized to an arbitrary number of qubits. The dashed line in the middle separates the two blocks of each Hamiltonian.

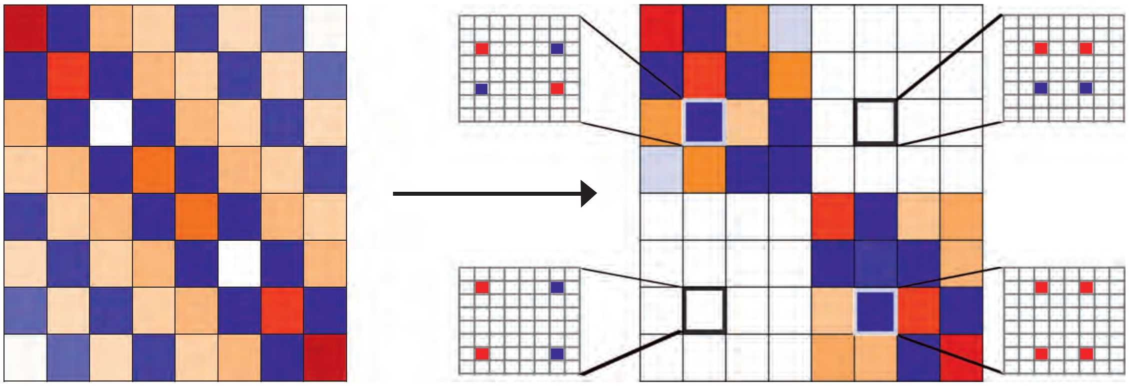

Fig. 11 An illustration of the block-diagonalization of the nuclear Hamiltonian, as captured by Eq. (17). The original Hamiltonian, $\mathcal{H}^{Mol}$ is on the left, whereas the transformed $\tilde{\mathcal{H}}_{il}^{Mol}$ is shown on the right. On the right side, specific matrix elements from each block of $\tilde{\mathcal{H}}_{il}^{Mol}$ are highlighted to illustrate Eqs. (18) and (19). These highlighted elements of $\tilde{\mathcal{H}}_{il}^{Mol}$ are obtained by combining elements of $\mathcal{H}^{Mol}$, as per Eq. (17), and these are marked using red and blue squares in zoomed in representations matrix elements in $\mathcal{H}^{Mol}$. The blue (negative) and red (positive) indicate the phase of the corresponding elements of $\mathcal{H}^{Mol}$, as obtained from α_i in Eqs. (17), (18) and (19).

columns of **Fig. 10**. Eqs. 15 and 16 form two mutually orthogonal subspaces and are represented in the top and bottom portions of **Fig. 10**, separated by the dashed line. These subspaces block diagonalize the nuclear Hamiltonian for symmetric potentials. This process is illustrated for a three-qubit system (2^3-grid points) in **Fig. 11**.

The il^{th} matrix element of the resultant molecular Hamiltonian in the Givens transformed grid basis is explicitly written as

$$\tilde{\mathcal{H}}_{il}^{Mol} = \frac{1}{2}\left(\mathcal{H}_{i,l}^{Mol} + \alpha_l \mathcal{H}_{i,n-l}^{Mol} + \alpha_i \mathcal{H}_{n-i,l}^{Mol} + (\alpha_i \alpha_l \mathcal{H}_{n-i,n-l}^{Mol}\right), \tag{17}$$

where $\alpha_i = \text{sgn}[i - (n/2)]$. The elements of the diagonal blocks of $\tilde{\mathcal{H}}^{Mol}$ (matrix on the right in **Fig. (11)**) are obtained from Eq. (17) as

$$\begin{aligned}\tilde{\mathcal{H}}_{il}^{Mol} &= \frac{1}{2}\left(\mathcal{H}_{i,l}^{Mol} + \alpha_i \mathcal{H}_{i,n-l}^{Mol} + \alpha_i \mathcal{H}_{n-i,l}^{Mol} + \mathcal{H}_{n-i,n-l}^{Mol}\right) \\ &= [K(x_i, x_l) + \alpha_i K(x_i, x_{n-l})] + = \frac{1}{2}[\mathrm{V}(x_i) + \mathrm{V}(x_{n-l})]\delta_{i,l}\end{aligned} \tag{18}$$

The elements of the unitary transform, α_i are, in fact, the characters of the C_s point group. The right hand side of the above equation, therefore, represents a symmetry adapted transformation of the nuclear Hamiltonian, and the term $\frac{1}{2}[\mathrm{V}(x_i) + \mathrm{V}(x_{n-i})]$, symmetrizes the potential energy surface in one-dimension. By extension, for the elements of the off-diagonal blocks of $\tilde{\mathcal{H}}^{Mol}$ in **Fig. 11**, $\alpha_l = -\alpha_i$ and

$$\begin{aligned}\tilde{\mathcal{H}}_{il}^{Mol} &= \frac{1}{2}\left(\mathcal{H}_{i,l}^{Mol} - \alpha_i \mathcal{H}_{i,n-l}^{Mol} + \alpha_i \mathcal{H}_{n-i,l}^{Mol} - \mathcal{H}_{n-i,n-l}^{Mol}\right) \\ &= \frac{1}{2}[\mathrm{V}(x_i) - \mathrm{V}(x_{n-l})]\delta_{i,n-l}\end{aligned} \tag{19}$$

where the kinetic energy contribution is identically zero purely due to the Toeplitz nature of Eq. (14), and only the anti-symmetric portion of the potential, $\frac{1}{2}[\mathrm{V}(x_i) - \mathrm{V}(x_{n-l})]$, contributes to the anti-diagonal part of $\tilde{\mathcal{H}}^{Mol}$. Thus for symmetric potentials such as those considered here, Eq. (19) is identically zero. This observation will become useful when we generalize the approach presented here, first to general potentials and then, to problems of higher dimensionality in future publications.

3.5 Mapping Protocol for Quantum Chemical Dynamics

The structure of the ion-trap Hamiltonian constrains the class of mappable problems. These constraints dictate the accuracy with which quantum chemical dynamics simulations can be performed on an ion-trap system given by Eq. (12). To summarize our discussion thus far (See **Fig. 10**), we began with a computational basis $|\lambda\rangle$, used to describe the Ising Hamiltonian, $\mathcal{H}_{IT}$ in Eq. (12), and the grid basis $|x\rangle$, used to represent the quantum nuclear Hamiltonian, $\mathcal{H}^{Mol}$ in Eq. (13). In the interest of matching the structures of the two Hamiltonians, we first obtained a permuted computational basis: $|\lambda\rangle \to |\tilde{\lambda}\rangle$ (Section 3.2, and also summarized on the right side of **Fig. 10**) and a unitary (Givens) transformed quantum nuclear basis: $|x\rangle \to |\tilde{x}\rangle$ (Section 3.4). In doing so our goal becomes:

$$\langle\tilde{x}|\mathcal{H}^{Mol}|\tilde{x}'\rangle \leftrightarrow \langle\tilde{\lambda}|\mathcal{H}_{\mathrm{IT}}|\tilde{\lambda}'\rangle \tag{20}$$

where we first introduce a map between the transformed quantum nuclear wavefunction bases and the permuted computational bases that represent the Ising spin lattice system as:

$$|\tilde{x}\rangle \Leftrightarrow |\tilde{\lambda}\rangle. \tag{21}$$

This map is illustrated within the central box in **Fig. 10** where the left side of the central box represents the Givens transformed grid basis, and the right side represents the permuted computational basis. Furthermore, the mapped basis states are separated into blocks by a dashed horizontal line. For the molecular Hamiltonian, the coupling across these blocks is identically zero for symmetric potentials, while for the Ising Hamiltonian, the coupling across these blocks is identically zero when the terms, B_i^x, B_i^y, are eliminated from Eq. (12) (See **Fig. 9**). The effectiveness of the maps in Eqs. (20) and (21) will essentially dictate the accuracy to which the dynamics captured within the ion-trap quantum simulator controlled by an Ising Hamiltonian accurately predicts the quantum nuclear dynamics.

In this section, we will show that, due to the structure of the Hamiltonians discussed in the previous sections, the diagonal and off-diagonal elements of each individual diagonal block of mappable Hamiltonians, such as Eq. (13), are Hadamard transformed to provide $\left\{B_i^z; J_{ij}^z\right\}$ and $\left\{J_{ij}^x; J_{ij}^y\right\}$, respectively. As a consequence of the discussion in Section 3.4, both Hamiltonians, Eqs. (12) and (13), by construction, take the form depicted in **Fig. 5**c and the right side of **Fig. 8**, respectively. We exploit this feature to evaluate a separate set of $\left\{B_i^z; J_{ij}^y\right\}$ values, below, for each of the two diagonal blocks of the molecular Hamiltonian, while maintaining $\left\{B_i^x; B_i^y\right\}$ to be identically zero.

3.6 Obtaining Ion-trap Parameters $\left\{B_i^z; J_{ij}^z\right\}$ From the Diagonal Elements of the Molecular Hamiltonian

The diagonal elements of the molecular Hamiltonian are directly mapped to those of the spin lattice Hamiltonian after invoking the map of the unitary transformed grid basis ($|\tilde{x}\rangle$) to the permuted computational basis ($|\tilde{\lambda}\rangle$). Each diagonal element of the molecular Hamiltonian in the transformed grid representation, $\tilde{x}|\mathcal{H}^{Mol}|\tilde{x}\rangle$, is equivalent to the corresponding element of the ion-trap Hamiltonian, $\bar{\lambda}|\mathcal{H}_{\mathrm{IT}}|\tilde{\lambda}\rangle$ in the permuted computational basis representation. In doing so, the set of on-site and inter-site coupling parameters, $\left\{B_i^z; J_{ij}^z\right\}$, of the ion-trap that occur along the diagonal of $\mathcal{H}_{\mathrm{IT}}$ can be evaluated. The mapping expression between the diagonal elements of the molecular Hamiltonian and the corresponding elements of the ion-trap Hamiltonian may be written as

$$\bar{x}|\mathcal{H}^{Mol}|\tilde{x}\rangle \equiv \left\langle\tilde{\lambda}|\mathcal{H}_{\mathrm{IT}}|\tilde{\lambda}\right\rangle \tag{22}$$

Using Eq. (18) and Eq. (12), for the left and right sides of Eq. (22), we obtain

$$\begin{aligned}&[K(x_i,x_i) - K(x_i,x_{n-i})] + \frac{1}{2}[\mathrm{V}(x_i) + \mathrm{V}(x_{n-i})]\\ &= \sum_{j=1}^{N}(-1)^{\tilde{\lambda}_j}B_j^z + \sum_{j=1}^{N-1}\sum_{k>j}^{N}(-1)^{\tilde{\lambda}_j \oplus \tilde{\lambda}_k}J_{jk}^z\\ &\text{for } \ i \leq n/2\end{aligned} \tag{23}$$

$$\begin{aligned}&[K(x_i,x_i) + K(x_i,x_{n-i})] + \frac{1}{2}[\mathrm{V}(x_i) + \mathrm{V}(x_{n-i})]\\ &= \sum_{j=1}^{N}(-1)^{\tilde{\lambda}_j}B_j^z + \sum_{j=1}^{N-1}\sum_{k>j}^{N}(-1)^{\tilde{\lambda}_j \oplus \tilde{\lambda}_k}J_{jk}^z\\ &\text{for } \ i > n/2\end{aligned} \tag{24}$$

where $\oplus$ on the right side denotes the addition modulo 2, $\tilde{\lambda}_j$ is the j^{th} bit of the bit representation of $\tilde{\lambda}$ with values 0 or 1 for up- or down-spin, respectively, as shown in **Fig. 9**.

Thus, the diagonal elements of $\tilde{\mathcal{H}}^{Mol}$ to obtain ion-trap parameters $\left\{B_i^z, J_{ij}^z\right\}$. The expressions needed for this purpose are derived from Eqs. (23) and (24), $\left\{B_i^z; J_{ij}^z\right\}$ are specific[72] Hadamard transforms of $\langle\tilde{x}|\mathcal{H}^{Mol}|\tilde{x}\rangle$, that is,

$$\langle\tilde{x}|\mathcal{H}^{Mol}|\tilde{x}\rangle \overset{\text{Hadamard}}{\rightarrow} \left\{B_i^z; J_{ij}^z\right\} \tag{25}$$

While this map is general for arbitrary number of qubits, the linear transformations between $\langle\tilde{x}|\mathcal{H}^{Mol}|\tilde{x}\rangle$ and $\left\{B_i^z; J_{ij}^z\right\}$, are rank-deficient and error estimates are presented in Ref. 72 that apply for arbitrary number of qubits.

4 Reduction of Circuit Depth in Quantum Electronic Structure

In order to gauge the accuracy and reduction in computational complexity arising from our Graph-|Q⟩⟨C| method presented above, we have applied this approach to a range of hydrogen molecular cluster problems. These systems are critical for applications related to energy storage.[170–175] In particular, the safe and efficient storage[173,175–178] of molecular hydrogen is of paramount importance to potential developments in new fuel cell technologies.[179–181] Furthermore, the study of ortho- and para-hydrogen[182–187] at low-temperatures has been a fundamental challenge that has implications towards the study of exotic new states of matter that may have important applications in low-temperature physics.[188–190]

While the key properties of such systems involve the detailed study of electronic as well as nuclear degrees of freedom,[191] with quantum algorithms for such applications discussed in Section 3, here we discuss the accuracy of Graph-|Q⟩⟨C| and its ability to reduce the complexity of quantum circuits in obtaining UCCSD level electronic energies for such systems.

Hydrogen molecular clusters of various sizes $(\mathrm{H}_2)_n$, ($\mathrm{n} = 2, \cdots, 128$) (**Fig. 12**) have been treated with the Graph-|Q⟩⟨C| method to demonstrate scalability and accuracy as the system size grows. Specifically, the analysis of errors due to the truncation in rank ($\mathcal{R}$ in Eq. (7)) and edge length cutoff used in the graph definition, allows us to gauge the fragment circuit complexity needed to achieve an acceptable (milli-Hartree) level of accuracy.

The complexity of our algorithm is determined by the maximum value of $\mathcal{R}$ within the family of quantum circuits: $\{\mathcal{U}_{\alpha,r}|_{r=0\cdots\mathcal{R}}\}$. Furthermore, these graph-based circuit complexities are also dictated by the maximum edge length that is used to create the graphs. In Ref. 83 a detailed analysis of the accuracy of Graph-|Q⟩⟨C| is conducted when both the maximum edge length as well as $\mathcal{R}$ are varied and chosen to have values up to their respective maximum possible values. Here we summarize the milli-Hartree level agreement between full UCCSD calculations and those obtained from Graph-|Q⟩⟨C|.

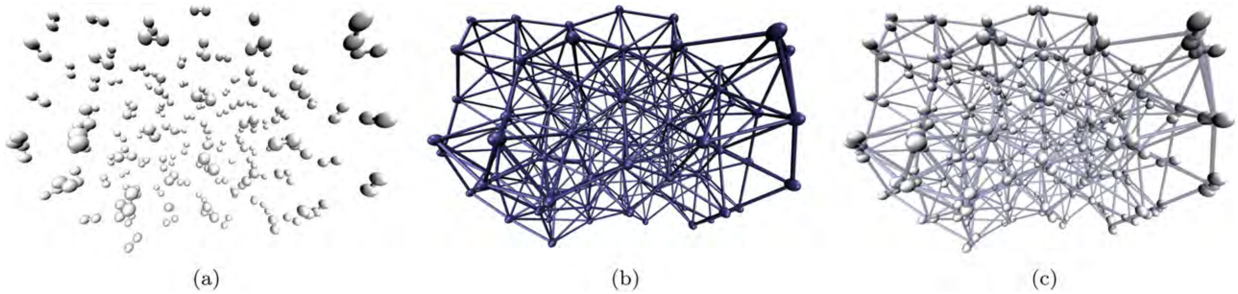

Fig. 12 Figure visually shows the drastically increasing number of fragments with increasing $\mathcal{R}$. Figure (a): $[\mathrm{H}_2]_{128}$. Figure (b): Graphical decomposition of $[\mathrm{H}_2]_{128}$, where each H_2 molecule is treated as a node, and edges connect all nodes within a 4.0 Å distance. Clearly as $\mathcal{R}$ increases, including edges, faces and higher order simplexes leads to a catastrophic growth in the number of fragments. Figure (c) combines the atomic and graph images.

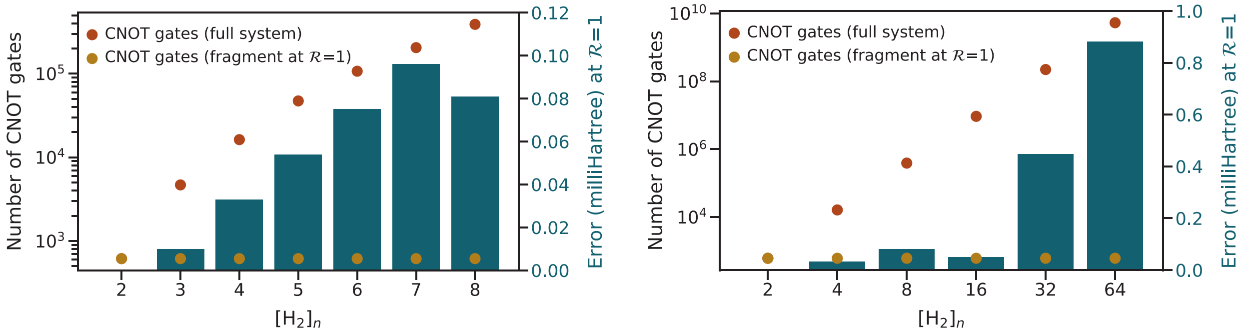

(a) (b)

Fig. 13 Results for larger H_2-clusters. Figure (a) and (b): 4.0 Å and $\mathcal{R} = 1$.

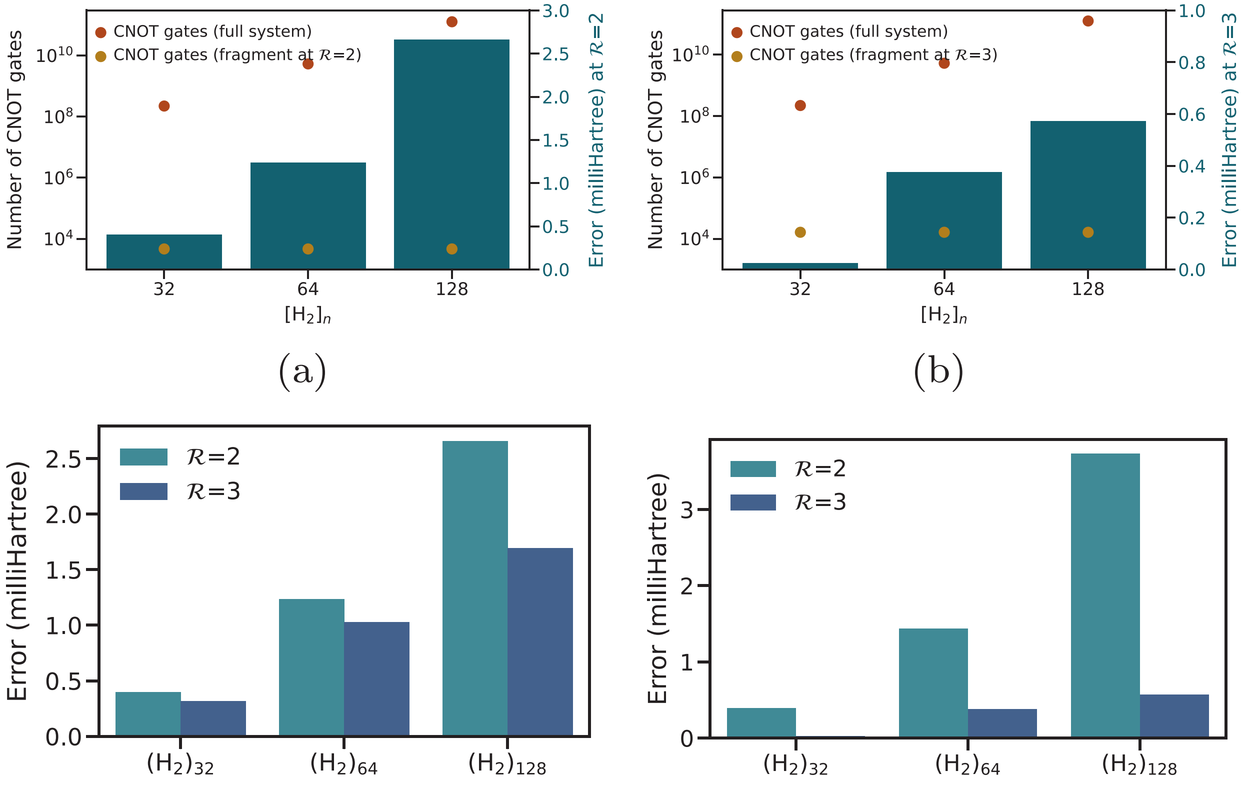

(a) (b)

(c) (d)

Fig. 14 Results for larger H_2-clusters. Figure (a): 4.0 Å and $\mathcal{R} = 2$. Figure (b): 7.5 Å and $\mathcal{R} = 3$. Figure (c): 4.0 Å and $\mathcal{R} = 2, 3$. Figure (d): 7.5 Å and $\mathcal{R} = 2, 3$. These figures show the progressive improvement in accuracy (Figures (c) and (d)) and the associated increase in costs (see relative vertical position of yellow dots on Figures (a) and (b)).

The set of results for larger H_2-clusters are presented in **Figs. 13** and **14**. While **Fig. 13**(a) summarizes the results for $[H_2]_n$ clusters, with $n = 1, \cdots 8$, **Fig. 13**(b) extends this out to $[H_2]_{64}$. As the size of the molecular system grows, the corresponding circuit complexity, as represented by the number of CNOT gates (red dots), increases exponentially. However, the complexity of Graph-|Q⟩⟨C|, as represented by the yellow dots in **Fig. 13**, grows in a gradual fashion while maintaining accuracy in the milli-Hartree range as can be seen from the right vertical axis of **Fig. 13**. Clearly these figures also show that while $\mathcal{R} = 1$ appears sufficient and does provide accurate results, the error grows with system size. Thus in **Figs. 10**(a) and (b) we present the accuracy, and CNOT-gate count for $\mathcal{R} = 2$ and $\mathcal{R} = 3$. Clearly increasing the value of $\mathcal{R}$ reduces the error but also increases the number of CNOT gates as seen in **Figs. 14**(c) and (d).

Table 1 Quantum circuit resource requirements when standard techniques are used: illustration for a family of H_2-clusters. Clearly as system size grows the circuit gets extremely complex. The Graph-$|Q\rangle\langle C|$ approach reduces resource complexity by several orders of magnitude

System	*Circuit depth*	*Number of qubits*	*Number of CNOT gates*	*Total number of gates*	*Number of parameters*
H_2	11	2	3	16	3
$(H_2)_2$	924	6	615	1217	26
$(H_2)_3$	5920	10	4684	7370	117
$(H_2)_4$	21,361	14	16,285	27,021	360
$(H_2)_5$	57,402	18	47,312	70,204	875
$(H_2)_6$	128,469	22	107,190	156,081	1818
$(H_2)_7$	253,846	26	205,192	313,143	3381
$(H_2)_8$	458,233	30	389,472	550,279	5792

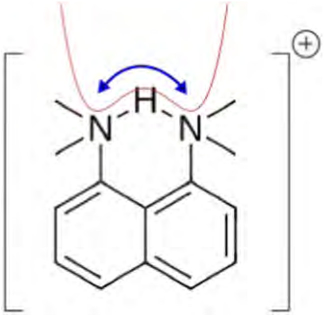

Fig. 15 The molecular geometry for DMANH$^+$ with the shared proton potential surface shown in red. The quantum mechanical nature of the shared proton allows it to be simultaneously present in both wells, and here we use Eq. (12) to simulate the behavior of this shared proton through our mapping protocol in Eq. (20).

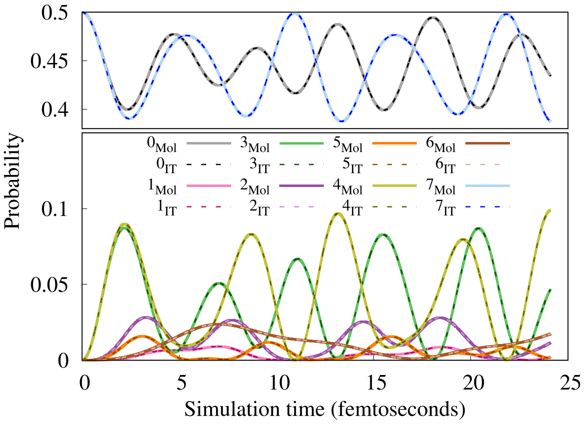

Fig. 16 Dynamics of the molecular and the ion trap systems: The integer (i) depicts the projection of a propagated state onto the i^{th} permuted spin basis state, $|\tilde{\lambda}_i\rangle$, and the corresponding Givens transformed grid basis state, $|\tilde{x}_i\rangle$, for the ion-trap (dashed) and the molecular system with $d_{DA} = 2.53$Å (solid), respectively. Note that all propagation is conducted on classical platforms. The agreement of the quantum dynamics in both systems is exact to within numerical round-off (10^{-15}). The two rows in the figure legend represent the two sets spanned by odd and even spin raising operators, $\{S^+\}$ acting on the $|\downarrow\downarrow\cdots\rangle$ spin state (dashed) and their corresponding Givens transformed grid basis states (solid) according to Eq. (21). An extended set of d_{DA} are considered in reference Saha, D., Iyengar, S.S., Richerme, P., Smith, J.M., Sabry, A., 2021. Mapping quantum chemical dynamics problems to spin-lattice simulators. J. Chem. Theory Comput. 17, 6713-6732, and results for a longer-term dynamics for the most stable structure ($d_{DA} = 2.53$Å) is provided in **Fig. 17**.

A more complete picture of circuit complexity can be seen from **Table 1**, where we present the circuit depth, the number of qubits, the number of CNOT gates, total number of gates, and number of parameters needed to describe a quantum circuit, using the standard implementation available in Qiskit, for clusters of various sizes. Thus, as per **Fig. 13**, when $\mathcal{R} = 1$ is used for these calculations the resources needed are as dictated by the second and third rows in **Table 1**. This provides a significant reduction in the resources needed to perform these computations, and as noted in the figures above.

Thus in general, choice of maximum $\mathcal{R}$ and edge length cut-off would be based on a compromise between the desired accuracy and efficiency. However, in all cases, it appears that Graph-$|Q\rangle\langle C|$ presents a powerful mode to adaptively tailor the quantum circuit depth problem.

5 Performance of the Mapping Protocol for Quantum Nuclear Dynamics: Case Study of a Symmetric Hydrogen Bonded System

We examine the map in Section 3 by simulating the quantum dynamics of the molecular system and the ion-trap dynamics, on classical hardware, independently. Analogous experimental studies on ion-trap quantum systems have been conducted[192] and are in review; these are in excellent agreement with the theoretical results discussed here. In doing so we study the time-evolution of the initial wavepacket

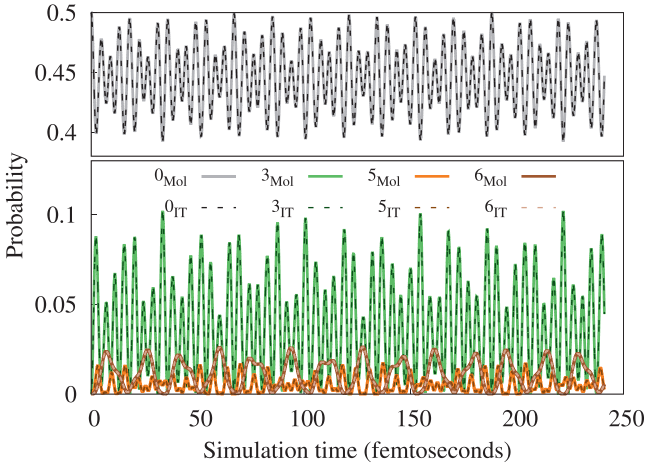

(a)Projections of the time-dependent wavepackets onto Block I vectors

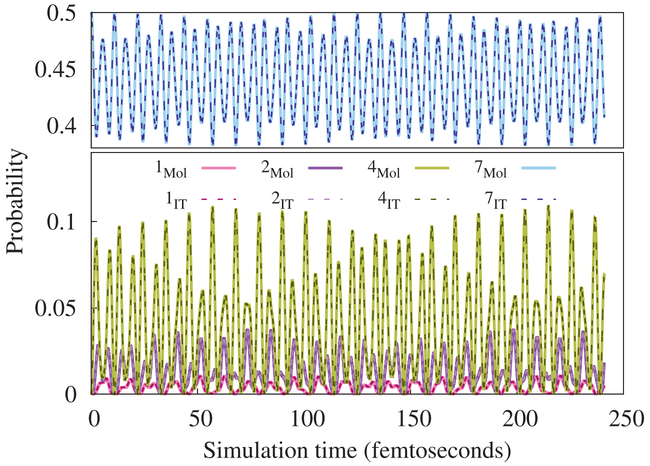

(b)Projections of the time-dependent wavepackets onto Block II vectors

Fig. 17 The dynamics of the molecular system (solid) and the ion-trap system (dashed) that show their exact match to within numerical round-off (10^{-15}) over long simulation times sufficient to capture the molecular vibrational properties. The projection of the respective time-dependent wavepackets onto basis vectors within each of the two decoupled blocks are shown separately for clarity.

states prepared in the respective permuted basis representations for the molecular and Ising model Hamiltonians. As stated, the parameters in the Ising Hamiltonian are determined, and thus controlled, by the pre-computed matrix elements of the molecular Hamiltonian. The specific intra-molecular proton transfer problem considered here is that in the protonated 1,8-bis(dimethylamino) naphthalene (DMANH^+) system shown in **Fig. 15**(a). The DMAN molecule has an extremely large proton affinity of 242 kcal/mol,[193] with $\mathrm{DMANH}^+ pK_a$ value in the range 12.1–12.3.[194]As a result, the system is one of the most frequently investigated proton sponges. The NHN^+ hydrogen bond in proton sponges is attractive from the point of view of both the nature of the short potentially symmetric hydrogen-bond bridges,[195–198] their infrared spectroscopic behavior and their propensity to occur in common nitrogen activation catalysts.[199,200] Thus, the DMANH^+ system has been frequently studied as a model for short, low-barrier hydrogen bonds that have a role in certain enzyme-catalyzed reactions. In solution, the shared proton delocalization in DMANH^+ is controlled by a low-barrier symmetric double-well potential, with barrier height being influenced by solvent and temperature.[201,202]

In the following subsections, we classically pre-compute the nuclear Hamiltonian for the system in **Fig. 15**, and simulate the quantum nuclear dynamics on these potentials using the Ising model based ion-trap simulators. We treat the shared proton stretch dimension within the Born-Oppenheimer limit. The nuclear Hamiltonian is determined by the ground electronic state potential energy surface.

6 Quantum Simulation of Proton-Transfer Dynamics

Given the block structure of both molecular and Ising Hamiltonians in the permuted and Givens transformed basis representations, the initial wavepacket for the ion-trap system is chosen as a coherent linear combination of the spin basis states: $\{|\uparrow\uparrow\uparrow\rangle + |\downarrow\downarrow\downarrow\rangle\sqrt{2}\}$ on a three qubit system. Given the block structure of the Ising Hamiltonian with $\{B_i^x, B_i^y\}$ turned off, the components of this initial state, $|\uparrow\uparrow\uparrow\rangle$ and $|\downarrow\downarrow\downarrow\rangle$, are not coupled. Additionally, these states will not couple such as might be the case in the presence of $B_3^x - iB_3^y$ in the off-diagonal blocks: for example, pathways such as $|\downarrow\downarrow\downarrow\rangle \overset{B_3^x - iB_3^y}{\longrightarrow} |\uparrow\downarrow\downarrow\rangle \overset{J_{12}^x - J_{12}^y}{\longrightarrow} |\uparrow\uparrow\uparrow\rangle$ will remain unpopulated. Hence, in essence, $|\uparrow\uparrow\uparrow\rangle$ gets propagated as per the unitary evolution corresponding to the top diagonal block of the Ising Hamiltonian and $|\downarrow\downarrow\downarrow\rangle$ as per the bottom-block. This critical feature allows us to treat the two separated blocks as arising from two different ion-traps with two different sets of $\left\{B_i^\gamma; J_{ij}^\gamma\right\}$ parameters. Given the direct map in Eq. (21) between the permuted computational basis and the Givens transformed molecular grid basis, the initial wavepacket for the molecular system is to be chosen in an analogous fashion to the initial wavepacket of the ion-trap, which is $\left\{\frac{|\tilde{x}_0\rangle + |\tilde{x}_7\rangle}{\sqrt{2}}\right\}$. This essentially leads to the initial wavepacket for the quantum nuclear dynamics problem as being chosen on one end of the grid, that is, a state localized closer to one of the nitrogen atoms in **Figs. 5**(a) and **10**(a). This choice results in the initial nuclear wavepacket being symmetrically located at either end of the Givens transformed basis (Eq. (16)). The spin-lattice and molecular wavepackets are then independently propagated for each potential obtained for different donor-acceptor separations, and compared to gauge accuracy of the quantum simulation.

Given the recursive form of the matrix representation of the Ising Hamiltonian in Eq. (12), as discussed in Ref. 72, the ion-trap hardware initial wavepacket state is directly propagated by the choice of $\left\{B_i^\gamma; J_{ij}^\gamma\right\}$ for arbitrary time-segments. While here, we emulate the time-evolution of the ion-trap system according to the Hamiltonian in Eq. (12) on classical hardware, by using the eigenstates of the Ising Hamiltonian in a publication under review[192] we have experimentally demonstrated the results here by performing quantum computations on an ion-trap system. The time-dependent probabilities resulting from the projection of the resultant time-dependent wavepacket on the computational basis, at each interval of time, is shown using dashed lines in **Figs. 16** and **17** for a donor-acceptor distance value of 2.53Å (The donor-acceptor distance value of 2.53Å corresponds to the most stable structure, but there are several other geometries that are also populated (at 300 K) even from a purely classical Boltzmann estimation). Hence these other geometries have also been discussed in detail in Ref. 72 Similarly, we determine the time-evolution of the initial wavepacket for the molecular system by using the eigenstates of the transformed Hamiltonian in Eq. (17), and the resulting probabilities from the projection of the time-dependent wavepacket on the Givens transformed grid basis, $\{|\tilde{x}\rangle\}$ are shown using solid lines in **Figs. 16**, and **17**. The probabilities match exactly, apart from numerical round-off error (10^{-15}), for the quantum simulation of the dynamics of the two systems. Clearly, this is also true for much longer time intervals as can be seen in **Fig. 17**. Given the exact match between the spin-lattice dynamics and the quantum chemical dynamics, the features present in ion-trap dynamics must also exist in the chemical dynamics problem. Thus through the isomorphism constructed above, our algorithm allows the ability to probe any entanglement that may be present in chemical systems.

7 Conclusions

The promise of solving exponentially complex problems efficiently using quantum computing hardware and associated quantum computing algorithms is a rapidly evolving research frontier.[25] While we are in the early stages of this quantum revolution, there are a wide set of scientific and technological areas that can benefit from such developments. However, true progress in such areas can only be achieved by a rigorous study and understanding of the electronic structure and dynamics of complex materials, thus requiring accurate treatment of electron correlation effects in conjunction with a rigorous treatment of quantum nuclear effects.[9,18,148,149,200,203,204]

Here, we discuss novel (a) procedures to reduce the depth of quantum circuits and reduce the extent to which this influences the quality of results in computing post-Hartree Fock electronic structure energies, and (b) general, but approximate mapping procedures between a quantum chemical dynamics problem, constructed on a single Born-Oppenheimer surface, and an ion-trap quantum simulator where the dynamics is dictated by a generalized form of the Ising model Hamiltonian.

The circuit depth reduction method is based on molecular fragmentation and specifically a molecular system is divided into overlapping fragments through a graph theoretic technique. This then allows the construction of a series of projection operators, that allow some overall model for quantum computing obtained from an approximation to the unitary evolution of the full system, into separate processes, some of which can be treated on quantum hardware and others on classical hardware. Thus, we discuss a procedure for electronic structure that can be spawned on to a potentially large ensemble of classical and quantum hardware systems. We also show that such a circuit decomposition approach yields up to *nine orders of magnitude reduction* in the number of CNOT gates and circuit depth for the larger sized clusters when compared to a standard quantum circuit implementation as available within Qiskit with limited loss in accuracy.

The key step involved in facilitating our map for the quantum nuclear dynamics problem is the partitioning of the coupled qubit space into two zones using only odd or even powers of the total spin raising operators that are used to generate such a coupled qubit space. Once the coupled qubit basis set is partitioned in such a way, the Ising model Hamiltonian reduces into a block form thus allowing the possibility to map *all* problems that may be written in a similar block form. We consider a symmetric proton-transfer problem and show how such a problem can be mapped to an ion-trap system, and also show that the dynamics of the two systems is *identical* provided the parameters of the ion trap are chosen in concert with that of the molecular system obtained from classical pre-computation.

General quantum nuclear dynamics problems, however, have unsymmetric potential energy surfaces and are generally performed in higher dimensions. Thus critical extensions to these methodologies using tensor networks are currently underway.

Acknowledgments

This research was supported by the National Science Foundation grants CHE-2102610 and OMA-1936353 to author S.S.I.

References

1. Iannuzzi, M., Parrinello, M., 2004. Proton transfer in heterocycle crystals. Phys. Rev. Lett. 93, 025901.
2. Tse, Y.-L.S., Herring, A.M., Kim, K., Voth, G.A., 2013. Molecular dynamics simulations of proton transport in 3M and nafion perfluorosulfonic acid membranes. J. Phys. Chem. C 117, 8079.
3. Lin, I.-H., Lu, Y.-H., Chen, H.-T., 2017. Nitrogen-doped C_{60} as a robust catalyst for CO oxidation. J. Comp. Chem. 38, 2041–2046.
4. Field, C., Bash, P.A., Karplus, M., 1990. A combined quantum mechanical and molecular mechanical potential for molecular dynamics simulations. J. Comput. Chem. 11, 700.
5. Wong, K.-Y., Gao, J., 2011. Insight into the phosphodiesterase mechanism from combined QM/MM free energy simulations. The FEBS J. 278, 2579–2595.
6. Harris, D.L., 2002. Oxidation and electronic state dependence of proton transfer in the enzymatic cycle of cytochrome P450eryF. J. Inorg. Biochem. 91, 568.
7. Lin, Y.-I, Gao, J., 2011. Kinetic isotope effects of L-dopa decarboxylase. J. Am. Chem. Soc. 133, 4398.
8. Rega, N., Iyengar, S.S., Voth, G.A., *et al.*, 2004. Hybrid ab-initio/empirical molecular dynamics: Combining the ONIOM scheme with the atom-centered density matrix propagation (ADMP) approach. J. Phys. Chem. B 108, 4210.
9. Iyengar, S.S., Sumner, I., Jakowski, J., 2008. Hydrogen tunneling in an enzyme active site: A quantum wavepacket dynamical perspective. J. Phys. Chem. B 112, 7601.
10. Phatak, P., Sumner, I., Iyengar, S.S., 2012. Gauging the flexibility of the active site in soybean lipoxygenase-1 (SLO-1) through an atom-centered density matrix propagation (ADMP) treatment that facilitates the sampling of rare events. J. Phys. Chem. B 116, 10145.
11. Gerber, R.B., Sebek, J., 2009. Dynamics simulations of atmospherically relevant molecular reactions. Int. Revs. Phys. Chem. 28, 207.
12. Dietrick, S.M., Pacheco, A.B., Phatak, P., Stevens, P.S., Iyengar, S.S., 2012. The influence of water on anharmonicity, stability and vibrational energy distribution of hydrogen-bonded adducts in atmospheric reactions: Case study of the OH + isoprene reaction intermediate using *ab-initio*. Molecular Dynamics. J. Phys. Chem. A 116, 399.
13. Hammerich, A.D., Finlayson-Pitts, B.J., Gerber, R.B., 2012. NOx reactions on aqueous surfaces with gaseous HCl: Formation of a potential precursor to atmospheric Cl atoms. J. Phys. Chem. Lett. 3, 3405–3410.
14. Head-Gordon, M., Pople, J.A., Frisch, M.J., 1988. MP2 energy evaluation by direct methods. Chem. Phys. Lett. 153, 503.
15. Schlegel, H.B., Frisch, M.J., 1991. Computational bottlenecks in molecular orbital calculations. Theoretical and Computational Models for Organic Chemistry. Springer. pp. 5–33.
16. Pople, J.A., Schlegel, H.B., Raghavachari, K., *et al.*, 1981. Molecular orbital studies of vibrational frequencies. Int. J. Quantum Chem. Quant. Chem. Symp. S15, 269–278.
17. Pople, J.A., Raghavachari, K., Schlegel, H.B., Binkley, J.S., 1979. Derivative studies in Hartree-Fock and Møller-Plesset theories. Int. J. Quantum Chem. Quant. Chem. Symp. S13. (225-41).
18. Raghavachari, K., Trucks, G.W., Pople, J.A., Head-Gordon, M., 1989. A fifth-order perturbation comparison of electron correlation theories. Chem. Phys. Lett. 157, 479–483v.
19. Feynman, R.P., Hibbs, A.R., Styer, D.F., 2010. Quantum mechanics and path integrals. Courier Corporation.
20. Ayala, P.Y., Scuseria, G.E., 1999. Linear scaling second-order Moller-Plesset theory in the atomic orbital basis for large molecular systems. J. Chem. Phys. 110, 3660–3671.
21. Schuütz, M., Hetzer, G., Werner, H.-J., 1999. Low-order scaling local electron correlation methods. I. Linear scaling local. J. Chem. Phys. 111, 5691–5705.
22. Distasio, R.A., Steele, R.P., Rhee, Y.M., Shao, Y., Head-Gordon, M., 2007. An improved algorithm for analytical gradient evaluation in resolution-of-the-identity second-order Møller-Plesset perturbation theory: Application to alanine tetrapeptide conformational analysis. J. Comput. Chem. 28, 839–856.
23. Pavośević, F., Pinski, P., Riplinger, C., Neese, F., Valeev, E.F., 2016. SparseMaps systematic infrastructure for reduced-scaling electronic structure methods. IV. Linear-scaling second-order explicitly correlated energy with pair natural orbitals. J. Chem. Phys. 144, 144109.

24. Sode, O., Hirata, S., 2012. Second-order many-body perturbation study of solid hydrogen fluoride under pressure. Phys. Chem. Chem. Phys. 14, 7765–7779.
25. Preskill, J., 2018. Quantum computing in the NISQ era and beyond. Quantum 2, 79.
26. Chia, N.-H., Chung, K.-M., Lai, C.-Y., 2020. On the Need for Large Quantum Depth. In: Proceedings of the 52nd Annual ACM SIGACT Symposium on Theory of Computing. STOC 2020, pp. 902–915. New York, NY: Association for Computing Machinery.
27. Porras, D., Cirac, J.I., 2004. Effective quantum spin systems with trapped ions. Phys. Rev. Lett. 92, 207901.
28. Richerme, P., Gong, Z.-X., Lee, A., *et al*., 2014. Non-local propagation of correlations in quantum systems with long-range interactions. Nature 511, 198.
29. Cirac, J.I., Zoller, P., 1995. Quantum computations with cold trapped ions. Phys. Rev. Lett. 74, 4091–4094.
30. Richerme, P., 2016. Two-dimensional ion crystals in radio-frequency traps for quantum simulation. Phys. Rev. A 94, 032320.
31. Barends, R., Kelly, J., Megrant, A., *et al*., 2014. Superconducting quantum circuits at the surface code threshold for faulttolerance tolerance. Nature 508, 500–503.
32. Barends, R., Lamata, L., Kelly, J., *et al*., 2015. Digital quantum simulation of fermionic models with a superconducting circuit. Nat. Commun. 6, 1–7.
33. Lanyon, B.P., Whitfield, J.D., Gillett, G.G., *et al*., 2010. Towards quantum chemistry on a quantum computer. Nat. Chem. 2, 106–111.
34. Aspuru-Guzik, A., Walther, P., 2012. Photonic quantum simulators. Nat. Phys. 8, 285–291.
35. Knill, E., Laflamme, R., Milburn, G.J., 2001. A scheme for efficient quantum computation with linear optics. Nature 409, 46–52.
36. Pellizzari, T., Gardiner, S.A., Cirac, J.I., Zoller, P., 1995. Decoherence, continuous observation, and quantum computing: A cavity QED model. Phys. Rev. Lett. 75, 3788.
37. Loss, D., DiVincenzo, D.P., 1998. Quantum computation with quantum dots. Phys. Rev. A 57, 120.
38. Imamoglu, A., Awschalom, D.D., Burkard, G., *et al*., 1999. Quantum information processing using quantum dot spins and cavity QED. Phys. Rev. Lett. 83, 4204.
39. Calarco, T., Datta, A., Fedichev, P., Pazy, E., Zoller, P., 2003. Spin-based all-optical quantum computation with quantum dots: Understanding and suppressing decoherence. Phys. Rev. A 68, 012310.
40. Saffman, M., Walker, T.G., Mølmer, K., 2010. Quantum information with Rydberg atoms. Rev. Mod. Phys. 82, 2313.
41. Saffman, M., 2016. Quantum computing with atomic qubits and Rydberg interactions: progress and challenges. J. Phys. B: Atomic Mol. Opt. Phys. 49, 202001.
42. Bernien, H., Schwartz, S., Keesling, A., *et al*., 2017. Probing many-body dynamics on a 51-atom quantum simulator. Nature 551, 579–584.
43. O’Malley, P.J.J., Babbush, R., Kivlichan, I.D., *et al*., 2016. Scalable quantum simulation of molecular energies. Phys. Rev. X 6, 031007.
44. Kandala, A., Mezzacapo, A., Temme, K., *et al*., 2017. Hardware-efficient variational quantum eigensolver for small molecules and quantum magnets. Nature 549, 242.
45. Xia, R., Kais, S., 2018. Quantum machine learning for electronic structure calculations. Nat. Commun. 9, 4195.
46. Gorman, D.J., Hemmerling, B., Megidish, E., *et al*., 2018. Engineering vibrationally assisted energy transfer in a trapped-ion quantum simulator. Phys. Rev. X 8, 011038.
47. Nam, Y., Chen, J.-S., Pisenti, N.C., *et al*., 2020. Ground-state energy estimation of the water molecule on a trapped ion quantum computer. npj Quantum Inf. 6, 33.
48. Wang, B.-X., Tao, M.-J., Ai, Q., *et al*., 2018. Efficient quantum simulation of photosynthetic light harvesting. npj Quantum Inf. 4.
49. Chin, A.W., Mangaud, E., Atabek, O., Desouter-Lecomte, M., 2018. Coherent quantum dynamics launched by incoherent relaxation in a quantum circuit simulator of a light-harvesting complex. Phys. Rev. A 97.
50. Potocnik, A., Bargerbos, A., Schroder, F.A.Y.N., *et al*., 2018. Studying light-harvesting models with superconducting circuits. Nat. Commun. 9.
51. Peruzzo, A., McClean, J., Shadbolt, P., *et al*., 2014. A variational eigenvalue solver on a photonic quantum processor. Nat. Commun. 5, 4213.
52. Grimsley, H.R., Economou, S.E., Barnes, E., Mayhall, N.J., 2019. An adaptive variational algorithm for exact molecular simulations on a quantum computer. Nat. Commun. 10, 1–9.
53. Arute, F., Arya, K., Babbush, R., *et al*., 2020. Hartree-Fock on a superconducting qubit quantum computer. Science 369, 1084–1089.
54. Parrish, R.M., Hohenstein, E.G., McMahon, P.L., Martinez, T.J., 2019. Quantum computation of electronic transitions using a variational quantum eigensolver. Phys. Rev. Lett. 122.
55. Tkachenko, N.V., Sud, J., Zhang, Y., *et al*., 2021. Correlation-informed permutation of qubits for reducing ansatz depth in the variational quantum eigensolver. PRX Quantum 2, 020337.
56. Cervera-Lierta, A., Kottmann, J.S., Aspuru-Guzik, A., 2021. Meta-variational quantum eigensolver: Learning energy profiles of parameterized hamiltonians for quantum simulation. PRX Quantum 2, 020329.
57. Huggins, W.J., McClean, J.R., Rubin, N.C., *et al*., 2021. Efficient and noise resilient measurements for quantum chemistry on near-term quantum computers. npj Quantum Inf. 7, 1–9.
58. McClean, J.R., Rubin, N.C., Sung, K.J., *et al*., 2020. OpenFermion: The electronic structure package for quantum computers. Quantum Sci. Technol. 5, 034014.
59. Motta, M., Gujarati, T.P., Rice, J.E., *et al*., 2020. Quantum simulation of electronic structure with a transcorrelated Hamiltonian: Improved accuracy with a smaller footprint on the quantum computer. Phys. Chem. Chem. Phys. 22, 24270–24281.
60. Lang, R.A., Ryabinkin, I.G., Izmaylov, A.F., 2021. Unitary transformation of the electronic Hamiltonian with an exact quadratic truncation of the Baker-Campbell-Hausdorff expansion. J. Chem. Theory Comput. 17, 66–78.
61. Ryabinkin, I.G., Yen, T.-C., Genin, S.N., Izmaylov, A.F., 2018. Qubit coupled cluster method: A systematic approach to quantum chemistry on a quantum computer. J. Chem. Theory Comput. 14, 6317–6326.
62. Izmaylov, A.F., Yen, T.-C., Lang, R.A., Verteletskyi, V., 2020. Unitary partitioning approach to the measurement problem in the variational quantum eigensolver method. J. Chem. Theory Comput. 16, 190–195.
63. Kirby, W.M., Love, P.J., 2021. Variational quantum eigensolvers for sparse Hamiltonians. Phys. Rev. Lett. 127, 110503.
64. Cervera-Lierta, A., Kottmann, J.S., Aspuru-Guzik, A., 2021. Meta-variational quantum eigensolver: Learning energy profiles of parameterized Hamiltonians for quantum simulation. PRX Quantum 2, 020329.
65. Kassal, I., Jordan, S.P., Love, P.J., Mohseni, M., Aspuru-Guzik, A., 2008. Polynomial-time quantum algorithm for the simulation of chemical dynamics. PNAS 105, 18681–18686.
66. MacDonell, R.J., Dickerson, C.E., Birch, C.J.T., *et al*., 2020. Analog quantum simulation of chemical dynamics.
67. Ollitrault, P.J., Baiardi, A., Reiher, M., Tavernelli, I., 2020. Hardware efficient quantum algorithms for vibrational structure calculations. Chem. Sci. 11, 6842–6855.
68. Sawaya, N.P., Menke, T., Kyaw, T.H., *et al*., 2020. Resource-efficient digital quantum simulation of d-level systems for photonic, vibrational, and spin-s Hamiltonians. npj Quantum Inf. 6, 1–13.
69. Teplukhin, A., Kendrick, B.K., Babikov, D., 2020. Solving complex eigenvalue problems on a quantum annealer with applications to quantum scattering resonances. Phys. Chem. Chem. Phys. 22, 26136–26144.
70. Jahangiri, S., Arrazola, J.M., Quesada, N., Delgado, A., 2020. Quantum algorithm for simulating molecular vibrational excitations. Phys. Chem. Chem. Phys. 22, 25528–25537.
71. Wang, C.S., Curtis, J.C., Lester, B.J., *et al*., 2020. Efficient multiphoton sampling of molecular vibronic spectra on a superconducting bosonic processor. Phys. Rev. X 10, 021060.
72. Saha, D., Iyengar, S.S., Richerme, P., Smith, J.M., Sabry, A., 2021. Mapping quantum chemical dynamics problems to spin-lattice simulators. J. Chem. Theory Comput. 17, 6713–6732.
73. Jordan, P., Wigner, E., 1928. Über das Paulische Äquivalenzverbot. Z. Phys. 47, 631–651.
74. Ortiz, G., Gubernatis, J.E., Knill, E., Laflamme, R., 2001. Quantum algorithms for fermionic simulations. Phys. Rev. A 64, 022319.
75. Bravyi, S.B., Kitaev, A.Y., 2002. Fermionic quantum computation. Ann. Phys. 298, 210–226.
76. Aspuru-Guzik, A., Dutoi, A.D., Love, P.J., Head-Gordon, M., 2005. Simulated quantum computation of molecular energies. Science 309, 1704.

77. Smart, S.E., Mazziotti, D.A., 2021. Quantum solver of contracted eigenvalue equations for scalable molecular simulations on quantum computing devices. Phys. Rev. Lett. 126, 070504.
78. Nielsen, M.A., Chuang, I.L., 2000. Quantum Computation and Quantum Information. New York, NY: Cambridge University Press.
79. Preskill, J., 2012. Quantum Computing and the Entanglement Frontier. arXiv:1203.5813 [quant-ph].
80. Aleksandrowicz, G., Alexander, T., Barkoutsos, P., *et al*., 2019. Qiskit: An open-source framework for quantum computing. https://doi.org/10.5281/zenodo.2562111.
81. Nam, Y., Chen, J.-S., Pisenti, N.C., *et al*., 2020. Ground-state energy estimation of the water molecule on a trapped-ion quantum computer. npj Quantum Inf. 6, 33.
82. Kandala, A., Wei, K.X., Srinivasan, S., *et al*., 2021. Demonstration of a high-fidelity cnot gate for fixed-frequency transmons with engineered ZZ suppression. Phys. Rev. Lett. 127, 130501.
83. Zhang, J.H., Iyengar, S.S., 2022. Graph-IQ> <CI: A graph-based Quantum-classical algorithm for efficient electronic structure on hybrid quantum/classical hardware systems: Improved quantum circuit depth performance. J. Chem. Theory Comput. 18, 2885.
84. Frisch, M.J., Trucks, G.W., Schlegel, H.B., *et al*., 2016. GaussianËœ16 Revision B.01. Wallingford, CT: Gaussian Inc.
85. Parrish, R.M., Burns, L.A., Smith, D.G.A., *et al*., 2017. PSI4 1.1: An open-source electronic structure program emphasizing automation, advanced libraries, and interoperability. J. Chem. Theor. Comput. 13, 3185.
86. Neese, F., 2012. The ORCA program system. Wiley Interdiscip. Rev. Comput. Mol. Sci. 2, 73.
87. Giannozzi, P., Baroni, S., Bonini, N., *et al*., 2009. QUANTUM ESPRESSO: A modular and open-source software project for quantum simulations of materials. J. Phys. Condens. Matt. 21, 395502.
88. Björklund, A., Husfeldt, T., Koivisto, M., 2009. Set partitioning via inclusion-exclusion. SIAM J. Comput. 39, 546.
89. Dey, T.K., Shah, N.R., 1997. On the number of simplicial complexes in R^d. Comput. Geom. 8, 267.
90. Adams, C.C., Franzosa, R.D., 2008. Introduction to topology: pure and applied.
91. Berger, M., Pansu, P., Berry, J.-P., Saint-Raymond, X., 1984. Affine spaces. Problems in Geometry. Springer. p. 11.
92. Ricard, T.C., Iyengar, S.S., 2020. An efficient and accurate approach to estimate hybrid functional and large basis set contributions to condensed phase systems and molecule-surface interactions. J. Chem. Theory Comput. 16, 4790.
93. Zhang, J.H., Ricard, T.C., Haycraft, C., Iyengar, S.S., 2021. Weighted-graph-theoretic methods for many-body corrections within ONIOM: Smooth AIMD and the role of high-order many-body terms. J. Chem. Theory Comput. 17, 2672–2690.
94. Li, J., Iyengar, S.S., 2015. Ab initio molecular dynamics using recursive, spatially separated, overlapping model subsystems mixed within an ONIOM based fragmentation energy extrapolation technique. J. Chem. Theory Comput. 11, 3978.
95. Li, J., Haycraft, C., Iyengar, S.S., 2016. Hybrid extended Lagrangian, post-Hartree-Fock Born-Oppenheimer ab initio molecular dynamics using fragment-based electronic structure. J. Chem. Theory Comput. 12, 2493.
96. Haycraft, C., Li, J., Iyengar, S.S., 2017. Efficient ,"On-the-Fly", Born–Oppenheimer and Car–Parrinello-type dynamics with coupled cluster accuracy through fragment based electronic structure. J. Chem. Theory Comput. 13, 1887.
97. Ricard, T.C., Haycraft, C., Iyengar, S.S., 2018. Adaptive, geometric networks for efficient coarse-grained ab initio molecular dynamics with post-Hartree-Fock accuracy. J. Chem. Theory Comput. 14, 2852.
98. Ricard, T.C., Iyengar, S.S., 2018. Efficiently capturing weak interactions in ab initio molecular dynamics through "on-the-fly" basis set extrapolation. J. Chem. Theory Comput. 14, 5535.
99. Kumar, A., Iyengar, S.S., 2019. Fragment-based electronic structure for potential energy surfaces using a superposition of fragmentation topologies. J. Chem. Theory Comput. 15, 5769.
100. Ricard, T.C., Kumar, A., Iyengar, S.S., 2020. Embedded, graph-theoretically defined many-body approximations for wavefunction-in-DFT and DFT-in-DFT: Applications to gas- and condensed-phase AIMD, and potential surfaces for quantum nuclear effects. Int. J. Quantum Chem. 120, e26244.
101. Kumar, A., DeGregorio, N., Iyengar, S.S., 2021. Graph-theory-based molecular fragmentation for efficient and accurate potential surface calculations in multiple dimensions. J. Chem. Theory Comput. 17, 6671–6690.
102. Kumar, A., DeGregorio, N., Ricard, T., Iyengar, S.S., 2022. Graph-theoretic molecular fragmentation for potential surfaces leads naturally to a tensor network form and allows accurate and efficient quantum nuclear dynamics. J. Chem. Theory Comput. 18, 7243.
103. Nyden, M., Petersson, G., 1981. Complete basis set correlation energies .1. The asymptotic convergence of pair natural orbital expasions. J. Chem. Phys. 75, 1843.
104. Pople, J., Head–Gordon, M., Fox, D., Raghavachari, K., Curtiss, L., 1989. Gaussian-1 theory: A general procedure for prediction of molecular energies. J. Chem. Phys. 90, 5622.
105. Montgomery, J., Frisch, M., Ochterski, J., Petersson, G., 1999. A complete basis set model chemistry. VI. Use of density functional geometries and frequencies. J. Chem. Phys 110, 2822.
106. DeYonker, N., Cundari, T., Wilson, A., 2006. The correlation consistent composite approach (ccCA): An alternative to the Gaussian-n methods. J. Chem. Phys. 124.
107. Raghavachari, K., Saha, A., 2015. Accurate composite and fragment-based quantum chemical models for large molecules. Chem. Rev. 115, 5643.
108. Maseras, F., Morokuma, K., 1995. IMOMM: A new integrated ab initio + molecular mechanics geometry optimization scheme of equilibrium structures and transition states. J. Comput. Chem. 16, 1170.
109. Kerdcharoen, T., Morokuma, K., 2002. ONIOM-XS: An extension of the ONIOM method for molecular simulation in condensed phase. Chem. Phys. Lett. 355, 257.
110. Hopkins, B.W., Tschumper, G.S., 2003. A multicentered approach to integrated QM/QM calculations. Applications to multiply hydrogen bonded systems. J. Com. Chem. 24, 1563.
111. Guo, W., Wu, A., Xu, X., 2010. XO: An extended ONIOM method for accurate and efficient geometry optimization of large molecules. Chem. Phys. Lett. 498, 203.
112. Mayhall, N.J., Raghavachari, K., 2011. Molecules-in-molecules: An extrapolated fragment-based approach for accurate calculations on large molecules and materials. J. Chem. Theory Comput. 7, 1336.
113. Mayhall, N.J., Raghavachari, K., 2012. Many-overlapping-body (MOB) expansion: A generalized many body expansion for nondisjoint monomers in molecular fragmentation calculations of covalent molecules. J. Chem. Theory Comput. 8, 2669.
114. Cervinka, C., Beran, G.J.O., 2018. Ab initio prediction of the polymorph phase diagram for crystalline methanol. Chem. Sci. 9, 4622.
115. Zhang, D.W., Zhang, J.Z.H., 2003. Molecular fractionation with conjugate caps for full quantum mechanical calculation of protein-molecule interaction energy. J. Chem. Phys 119, 3599.
116. Huang, L., Massa, L., Karle, J., 2005. Kernel energy method: Application to DNA. Biochemistry 44, 16747.
117. Ganesh, V., Dongare, R.K., Balanarayan, P., Gadre, S.R., 2006. Molecular tailoring approach for geometry optimization of large molecules: Energy evaluation and parallelization strategies. J. Chem. Phys. 125, 104109.
118. Jacobson, L.D., Herbert, J.M., 2011. An efficient, fragment-based electronic structure method for molecular systems: Self-consistent polarization with perturbative two-body exchange and dispersion. J. Chem. Phys. 134, 094118.
119. Richard, R.M., Herbert, J.M., 2012. A generalized many-body expansion and a unified view of fragment-based methods in electronic structure theory. J. Chem. Phys. 137, 064113.
120. Le, H.-A., Tan, H.-J., Ouyang, J.F., Bettens, R.P.A., 2012. Combined fragmentation method: A simple method for fragmentation of large molecules. J. Chem. Theory Comput. 8, 469.
121. Li, S., Li, W., Ma, J., 2014. Generalized energy-based fragmentation approach and its applications to macromolecules and molecular aggregates. Acc. Chem. Res. 47, 2712.

122. Gordon, M., Mullin, J., Pruitt, S., *et al.*, 2009. Accurate Methods for Large Molecular Systems. J. Phys. Chem. B 113, 9646.
123. Collins, M.A., Bettens, R.P.A., 2015. Energy-Based Molecular Fragmentation Methods. Chem. Rev. 115, 5607.
124. Collins, M.A., 2012. Systematic fragmentation of large molecules by annihilation. Phys. Chem. Chem. Phys. 14, 7744.
125. Willow, S.Y., Salim, M.A., Kim, K.S., Hirata, S., 2015. Ab initio molecular dynamics of liquid water using embedded-fragment second-order many-body perturbation theory towards its accurate property prediction. Sci. Rep. 5, 14358.
126. Han, J., Mazack, M.J.M., Zhang, P., Truhlar, D.G., Gao, J., 2013. Quantum mechanical force field for water with explicit electronic polarization. J. Chem. Phys. 139, 054503.
127. Liu, J., Qi, L.-W., Zhang, J.Z.H., He, X., 2017. Fragment quantum mechanical method for large-sized ion –water clusters. J. Chem. Theory Comput. 13, 2021.
128. Herbert, J.M., 2019. Fantasy versus reality in fragment-based quantum chemistry. J. Chem. Phys. 151, 170901.
129. Varandas, A.J., Murrell, J.N., 1977. A many-body expansion of polyatomic potential energy surfaces: Application to H_n systems. Faraday Discuss. Chem. Soc. 62, 92.
130. Murrell, J., Carter, S., Farantos, S., Huxley, P., Varandas, A., 1984. Molecular Potential Energy Functions. New York: Wiley.
131. Varandas, A., Pais, A., 1988. A realistic double many-body expansion (DMBE) potential energy surface for ground-state O_3 from a multiproperty fit to ab initio calculations, and to experimental spectroscopic, inelastic scattering, and kinetic isotope thermal rate data. Mol. Phys. 65, 843.
132. Xantheas, S.S., 1994. *Ab initio* studies of cyclic water clusters $(H_2O)_n$, N=1-6. II. Analysis of many body interactions. J. Chem. Phys. 100, 7523.
133. Xantheas, S.S., 1995. *Ab Initio* studies of cyclic water clusters $(H_2O)_n$, N=1-6. III. Comparison of density functional with MP2. Results. J. Chem. Phys. 102, 4505.
134. Dahlke, E.E., Truhlar, D.G., 2007. Electrostatically embedded many body expansion for large systems, with applications to water clusters. J. Chem. Theory Comput. 3, 46.
135. Dahlke, E.E., Truhlar, D.G., 2008. Electrostatically embedded many body expansion for simulations. J. Chem. Theory Comput. 4, 1.
136. Hirata, S.F., 2008. Electron-correlation methods for molecular crystals: An application to the α,β (1), and β (2) modifications of solid formic acid. J. Chem. Phys. 129, 204104.
137. Yu, Q., Bowman, J.M., 2017. Communication: VSCF/VCI vibrational spectroscopy of $H_7O_3^+$ and $H_9O_4^+$ using high-level, many-body potential energy surface and dipole moment surfaces. J. Chem. Phys. 146, 121102.
138. Yang, J., Hu, W., Usvyat, D., *et al.*, 2014. Ab initio determination of the crystalline benzene lattice energy to sub-kilojoule/mole accuracy. Science 345, 640.
139. Zhu, X., Iyengar, S.S., 2022. Graph theoretic molecular fragmentation for multidimensional potential energy surfaces yield an adaptive and general transfer machine learning protocol. J. Chem. Theory Comput. 18, 5125–5144.
140. Ozaki, T., Kino, H., Yu, J., *et al.*, 2016. User's manual of OpenMX Ver. 3.8.
141. Nash, B., Gheorghiu, V., Mosca, M., 2020. Quantum circuit optimizations for NISQ architectures. Quantum Sci. Technol. 5, 025010.
142. da Silva, R.D., Pius, E., Kashefi, E., 2013. Global quantum circuit optimization. arXiv preprint arXiv:1301.0351.
143. Bravyi, S., Gambetta, J.M., Mezzacapo, A., Temme, K., 2017. Tapering off qubits to simulate fermionic Hamiltonians. arXiv preprint arXiv:1701.08213.
144. Kraft, D., 1988. A software package for sequential quadratic programming; Wiss. Berichtswesen d. DFVLR Brunswick, Germany.
145. Zhang, D.-B., Yuan, Z.-H., Yin, T., 2020. Variational quantum eigensolvers by variance minimization. arXiv preprint arXiv:2006.15781.
146. Shen, Y., Zhang, X., Zhang, S., *et al.*, 2017. Quantum implementation of the unitary coupled cluster for simulating molecular electronic structure. Phys. Rev. A 95, 020501.
147. Grimsley, H.R., Claudino, D., Economou, S.E., Barnes, E., Mayhall, N.J., 2019. Is the trotterized uccsd ansatz chemically well-defined? J. Chem. Theory Comput. 16, 1–6.
148. Nagel, Z., Klinman, J., 2006. Tunneling and dynamics in enzymatic hydride transfer. Chem. Rev. 106, 3095.
149. Sumner, I., Iyengar, S.S., 2010. Analysis of hydrogen tunneling in an enzyme active site using Von Neumann measurements. J. Chem. Theory Comput. 6, 1698.
150. Xia, R., Bian, T., Kais, S., 2018. Electronic Structure Calculations and the Ising Hamiltonian. J. Phys. Chem. B 122, 3384–3395.
151. Bravyi, S., Hastings, M., 2017. On complexity of the quantum Ising model. Communications in Mathematical Physics 349, 1–45.
152. Copenhaver, J., Wasserman, A., Wehefritz-Kaufmann, B., 2021. Using quantum annealers to calculate ground state properties of molecules. J. Chem. Phys. 154, 034105.
153. Weinberg, D.R., Gagliardi, C.J., Hull, J.F., *et al.*, 2012. Proton-coupled electron transfer. Chem. Rev. 112, 4016–4093.
154. Nielsen, M.A., Chuang, I.L., 2000. Quantum Computation and Quantum Information. Cambridge: Cambridge University Press.
155. Golub, G.H., Van Loan, C.F., 2013. Matrix Computations. vol. 3. JHU press.
156. Britton, J.W., Sawyer, B.C., Keith, A.C., *et al.*, 2012. Engineered two-dimensional Ising interactions in a trapped-ion quantum simulator with hundreds of spins. Nature 484, 489–492.
157. Wang, Y., Um, M., Zhang, J., *et al.*, 2017. Single-qubit quantum memory exceeding ten-minute coherence time. Nat. Photon. 11, 646.
158. Mølmer, K., Sørensen, A., 1999. Multiparticle entanglement of hot trapped ions. Phys. Rev. Lett. 82, 1835.
159. Noek, R., Vrijsen, G., Gaultney, D., *et al.*, 2013. High speed, high fidelity detection of an atomic hyperfine qubit. Opt. Lett. 38, 4735–4738.
160. Ludlow, A.D., Boyd, M.M., Ye, J., Peik, E., Schmidt, P.O., 2015. Optical atomic clocks. Rev. Mod. Phys. 87, 637.
161. Blatt, R., Roos, C.F., 2012. Quantum simulations with trapped ions. Nat. Phys. 8, 277.
162. Islam, *et al.*, 2013. R. Emergence and frustration of magnetism with variable-range interactions in a quantum simulator. Science 340, 583–587.
163. Richerme, P., Senko, C., Smith, J., *et al.*, 2013. Experimental performance of a quantum simulator: Optimizing adiabatic evolution and identifying many-body ground states. Phys. Rev. A 88, 012334.
164. Senko, C., Smith, J., Richerme, P., *et al.*, 2014. Coherent imaging spectroscopy of a quantum many-body spin system. Science 345, 430–433.
165. Smith, J., Lee, A., Richerme, P., *et al.*, 2016. Many-body localization in a quantum simulator with programmable random disorder. Nat. Phys. 12, 907.
166. Zhang, J., *et al.*, 2017. Observation of a discrete time crystal. Nature 543, 217.
167. Tran, M.C., Guo, A.Y., Baldwin, C.L., 2021. The Lieb-Robinson light cone for power-law interactions.
168. Kouri, D.J., Huang, Y., Hoffman, D.K., 1995. Iterated real-time path integral evaluation using a distributed approximating functional propagator and average-case complexity integration. Phys. Rev. Lett. 75, 49.
169. Hoffman, D.K., Nayar, N., Sharafeddin, O.A., Kouri, D., 1991. Analytic banded approximation for the discretized free propagator. J. Phys. Chem. 95. 8299-8305.
170. Dillon, A., Jones, K., Bekkedahl, T., *et al.*, 1997. Storage of hydrogen in single-walled carbon nanotubes. Nature 386, 377–379.
171. Chambers, A., Park, C., Baker, R., Rodriguez, N., 1998. Hydrogen storage in graphite nanofibers. J. Phys. Chem. B 102, 4253–4256.
172. Dalebrook, A.F., Gan, W., Grasemann, M., Moret, S., Laurenczy, G., 2013. Hydrogen storage: Beyond conventional methods. Chem. Commun. 49, 8735–8751.
173. Niaz, S., Manzoor, T., Pandith, A.H., 2015. Hydrogen storage: Materials, methods and perspectives. Renew. Sust. Energ. Rev. 50, 457–469.
174. Ren, J., Musyoka, N.M., Langmi, H.W., Mathe, M., Liao, S., 2017. Current research trends and perspectives on materials-based hydrogen storage solutions: A critical review. Int. J. Hydrog. Energy 42, 289–311.
175. Gupta, A., Baron, G., Perreault, V., *et al.*, 2021. Hydrogen clathrates: Next generation hydrogen storage materials. Energy Storage Mater. 41, 69–107.
176. Mao, W., Mao, H., Goncharov, A., *et al.*, 2002. Hydrogen clusters in clathrate hydrate. Science 297, 2247–2249.
177. Patchkovskii, S., Tse, J., Yurchenko, S., *et al.*, 2005. Graphene nanostructures as tunable storage media for molecular hydrogen. Proc. Natl. Acad. Sci. USA 102, 10439–10444.
178. Granja-DelRio, A., Alducin, M., Inaki Juaristi, J., Lopez, M.J., Alonso, J.A., 2021. Length Absence of spillover of hydrogen adsorbed on small palladium clusters anchored to graphene vacancies. Appl. Surf. Sci. 559.
179. Edwards, P.P., Kuznetsov, V.L., David, W.I.F., Brandon, N.P., 2008. Hydrogen and fuel cells: Towards a sustainable energy future. Energy Policy 36, 4356–4362.
180. Tollefson, J., 2010. Hydrogen vehicles: fuel of the future? Nat. News 464, 1262–1264.
181. Dodds, P.E., Staffell, L., Hawkes, A.D., *et al.*, 2015. Hydrogen and fuel cell technologies for heating: A review. Int. J. Hydrog. Energy 40, 2065–2083.

182. Xu, M., Elmatad, Y.S., Sebastianelli, F., Moskowitz, J.W., Bacic, Z., 2006. Hydrogen molecule in the small dodecahedral cage of a clathrate hydrate: Quantum five-dimensional calculations of the coupled translation-rotation eigenstates. J. Phys. Chem. B 110, 24806–24811.
183. Turro, N.J., Mart, A.A., Chen, J.Y.-C., *et al.*, 2008. Demonstration of a chemical transformation inside a fullerene. The reversible conversion of the allotropes of H2@ C60. J. Am. Chem. Soc. 130, 10506.
184. Bacic, Z., Xu, M., Felker, P.M., 2018. Coupled translation–rotation dynamics of H_2 and H_2O inside C60: Rigorous quantum treatment. In: Whaley, K.B. (Ed.), Advances in Chemical Physics, vol. 163. Malden, MA: Wiley-Blackwell, pp. 195–216.
185. Tsuge, M., Namiyoshi, T., Furuya, K., *et al.*, 2021. Rapid ortho-to-para nuclear spin conversion of H-2 on a silicate dust surface. Astrophys. J. 908.
186. Bron, E., Le Petit, F., Le Bourlot, J., 2016. Efficient ortho-para conversion of H-2 on interstellar grain surfaces. Astron. Astrophys. 588.
187. Bezard, B., Vinatier, S., 2018. On the H-2 abundance and ortho-to-para ratio in Titan's troposphere. ICARUS 2020, 344, Cassini Science Symposium, Univ Colorado, Boulder, CO, AUG.
188. Lee, S., Park, K., Choi, Y., *et al.*, 2000. Hydrogen adsorption and storage in carbon nanotubes. Synth. Met. 113, 209–216.
189. Narehood, D., Kostov, M., Eklund, P., Cole, M., Sokol, P., 2002. Deep inelastic neutron scattering of H-2 in single-walled carbon nanotubes. Phys. Rev. B. 65.
190. Yamaoka, S., Hyeon-Deuk, K., 2021. Distinct molecular dynamics dividing liquid-like and gas-like supercritical hydrogens. Phys. Chem. Chem. Phys.
191. Deumens, E., Diz, A., Longo, R., Öhrn, Y., 1994. Time-dependent theoretical treatments of the dynamics of electrons and nuclei in molecular-systems. Rev. Mod. Phys. 66, 917.
192. Richerme, P., Revelle, M.C., Saha, D., *et al.*, 2022. Quantum Computation of Hydrogen Bond Dynamics and Vibrational Spectra. arXiv, https://arxiv.org/abs/2204.08571.
193. Lias, S.G., Liebman, J.F., Levin, R.D., 1984. Evaluated gas phase basicities and proton affinities of molecules; heats of formation of protonated. Mol. J. Phys. Chem. Ref. Data 13, 695–808.
194. Perrin, D.D., 1972. Dissociation Constants of Organic Bases in Aqueous Solution: Supplement 1972. vol. 1. Franklin Book Company.
195. Perrin, C.L., Nielson, J.B., 1997. 'Strong' hydrogen bonds in chemistry and biology. Ann. Revs. Phys. Chem. 48, 511.
196. Gerlt, J.A., Kreevoy, M.M., Cleland, W.W., Frey, P.A., 1997. Understanding enzymic catalysis: The importance of short, strong hydrogen bonds. Chem. Biol. 4, 259.
197. Warshel, A., Papazyan, A., Kollman, P.A., 1995. On low-barrier hydrogen-bonds and enzyme catalysis. Science 269, 102.
198. Cleland, W.W., Kreevoy, M.M., 1994. Low-barrier hydrogen-bonds and enzymatic catalysis. Science 264, 1887.
199. Yandulov, D.V., Schrock, R.R., 2002. Reduction of dinitrogen to ammonia at a well-protected reaction site in a molybdenum triamidoamine complex. J. Am. Chem. Soc. 124, 6252.
200. Harris, D.F., Lukoyanov, D.A., Shaw, S., *et al.*, 2018. The mechanism of N_2 reduction catalyzed by Fe-nitrogenase involves reductive elimination of H_2. Biochemistry 57, 701–710.
201. Perrin, C.L., 2010. Are short, low-barrier hydrogen bonds unusually strong? Acc. Chem. Res. 43, 1550–1557.
202. Pietrzak, M., Wehling, J.P., Kong, S., *et al.*, 2010. Symmetrization of cationic hydrogen bridges of protonated sponges induced by solvent and counteranion interactions as revealed by NMR spectroscopy. Chem. Eur. J. 16, 1679–1690.
203. Hammes-Schiffer, S., 2009. Theory of proton-coupled electron transfer in energy conversion processes. Acc. Chem. Res. 42, 1881–1889.
204. Mardirossian, N., Head-Gordon, M., 2017. Thirty years of density functional theory in computational chemistry: An overview and extensive assessment of 200 density functionals. Mol. Phys. 115, 2315–2372.